JACS
JOURNAL OF THE AMERICAN CHEMICAL SOCIETY

pubs.acs.org/JACS

Article

Elucidation of the pH-Dependent Electric Double Layer Structure at the Silica/Water Interface Using Heterodyne-Detected Vibrational Sum Frequency Generation Spectroscopy

Feng Wei, Shu-hei Urashima, Satoshi Nihonyanagi, and Tahei Tahara*

Cite This: J. Am. Chem. Soc. 2023, 145, 8833−8846

Read Online

ACCESS | Metrics & More | Article Recommendations | Supporting Information

ABSTRACT: The silica/water interface is one of the most abundant charged interfaces in natural environments, and the elucidation of the water structure at the silica/water interface is essential. In the present study, we measured the interface-selective vibrational ($\chi^{(2)}$) spectra in the OH stretch region of the silica/water interface in a wide pH range of pH 2.0−12.0 while changing the salt concentration by heterodyne-detected vibrational sum-frequency generation spectroscopy. With the help of singular value decomposition analysis, it is shown that the imaginary part of the $\chi^{(2)}$ ($\mathrm{Im}\chi^{(2)}$) spectra can be decomposed into the spectra of the diffuse Gouy−Chapman layer (DL) and the compact Stern layer (SL), which enables us to quantitatively analyze the spectra of DL and SL separately. The salt-concentration dependence of the DL spectra at different pH values is analyzed using the modified Gouy−Chapman theory, and the pH-dependent surface charge density and the pK_a value (4.8 ± 0.2) of the silica/water interface are evaluated. Furthermore, it is found that the pH-dependent change of the SL spectra is quantitatively explained by three spectral components that represent the three characteristic water species appearing in different pH regions in SL. The quantitative understanding obtained from the analysis of each spectral component in the $\mathrm{Im}\chi^{(2)}$ spectra provides a clear molecular-level picture of the electric double layer at the silica/water interface.

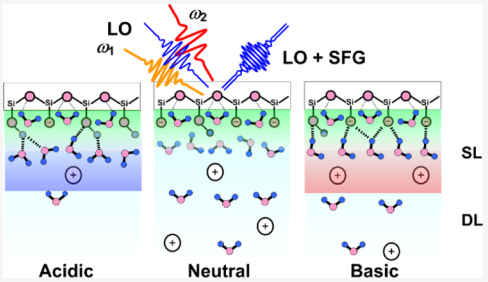

1. INTRODUCTION

The silica/water interface has attracted much attention and has been a subject of intensive studies because of its importance in many fundamental and applied research fields. From the fundamental viewpoint, the silica/water interface has been regarded as a prototypical model system for studying mineral/water interfaces as well as charged solid/water interfaces because of its abundance in the natural environment.[1] The silica/water interface is also involved in many applications, such as heterogeneous catalysis,[2] drug delivery,[3,4] and ion-sensitive sensors.[5] Therefore, molecular-level elucidation of the properties of the silica/water interface is essential for both a fundamental understanding of the silica surface and the application of silica-related materials.

The silica/water interface consists of water molecules, ions in the aqueous phase, and silica surface species such as silanol (SiOH) and bridge oxygen (Si−O−Si). Since the SiOH groups at the silica surface are deprotonated (SiO^-) under most pH conditions (>pH 2.0), the silica interface is usually negatively charged when in contact with water.[6,7] Consequently, the negatively charged silica surface attracts countercations in the aqueous phase, and an electrical double layer (EDL) is formed at the silica/water interface. For an interface with a low charge density and a dilute solution, the EDL structure can be well described by the Gouy−Chapman theory.[8,9] At the silica/water interface, however, the ion concentration can become high in the vicinity of the silica surface due to its high charge density (~0.87 e/nm^2),[9] making the assumptions of Gouy−Chapman theory invalid. Thus, the EDL is described by the Stern model, which consists of a compact Stern layer (SL) and a diffuse Gouy−Chapman layer (DL).[10,11] The elucidation of the structure and property of SL and DL is indispensable for a comprehensive understanding of EDL.

Many experimental[7,9,12−29] and theoretical studies[11,30−32] have been carried out to understand the properties of EDL at the charged surface. In addition to the conventional electrochemical scanning and electrocapillarity experiments,[13] many spectroscopic methods, such as X-ray absorption spectroscopy,[14] ambient pressure X-ray photoelectron spectroscopy,[15] second harmonic generation (SHG),[9,16−18] vibrational sum-frequency generation (VSFG) spectroscopy,[19−29] have been applied to gain molecular insights into the charged interface. Among these spectroscopic methods, VSFG spectroscopy is particularly useful because it can probe molecules within the EDL.[24−28] Several VSFG studies have shown that the SFG

Received: October 26, 2022
Published: April 17, 2023

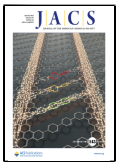

https://doi.org/10.1021/jacs.2c11344
J. Am. Chem. Soc. 2023, 145, 8833−8846

intensity at the silica/water interface decreases with the increase of the ionic strength, reflecting the decrease of net orientation of water molecules in DL due to the screening of the electric field that arises from the charge at the interface.[24,33,34] However, the molecular structures in SL and DL at the silica/water interface are still elusive because the conventional VSFG measurements can only provide the SFG intensity information, which is proportional to the modulus square of the molecular response, that is, the square of the second-order nonlinear susceptibility ($|\chi^{(2)}|^2$). Therefore, the sign of the nonlinear susceptibility ($\chi^{(2)}$) is lost, and the obtained vibrational spectrum is distorted due to the interference between different spectral components, including the non-resonant background. These drawbacks make it difficult to derive proper information about the silica/water interface from the VSFG spectra, even with the assistance of theory and computation.

To avoid the difficulties brought by the square nature of the conventional SFG intensity spectra, heterodyne-detected (HD-) VSFG techniques were developed to directly measure $\chi^{(2)}$ spectra.[35−40] The $\chi^{(2)}$ spectra obtained by HD-VSFG spectroscopy are linear to the nonlinear susceptibility. In particular, the imaginary part of the $\chi^{(2)}$ spectrum ($\mathrm{Im}\chi^{(2)}$) exhibits vibrational resonances with absorptive line shapes and is directly compared to the infrared and Raman spectra. Furthermore, spectral decomposition is readily achieved by model fitting[37] or simple subtractions,[40] making interpretation of the data straightforward. HD-VSFG spectroscopy has been applied for studying various aqueous interfaces, including buried interfaces such as the SiO_2/water interfaces.[37,39,40] In a pioneering study, Shen and co-workers observed three OH bands in the $\mathrm{Im}\chi^{(2)}$ spectrum at the quartz (0001)/water interface and discussed the interfacial water structures.[37] Later, our group measured the $\mathrm{Im}\chi^{(2)}$ spectra of the silica/water interface using H_2O and isotopically diluted water (HOD-D_2O) at pH 12.1, pH 7.2, and pH 2.1 and showed that the spectra at the silica/H_2O interface are significantly affected by the vibrational coupling.[39] We discussed the water structure at the silica/H_2O interface, as well as its pH-dependent change, based on the spectra at the silica/HOD-D_2O interface that are free from the vibrational coupling. However, a full picture of the EDL structure at the silica/water interface is still unclear because these early studies were performed with a low ion concentration, and hence they did not separately discuss SL and DL.

Several groups tried to decompose the VSFG ($|\chi^{(2)}|^2$) spectra at the silica/water interface into the spectra of the SL and DL, using various means such as theoretical modeling,[41] DFT-based molecular dynamics simulations,[42] and the maximum entropy method (MEM).[43] Nevertheless, such separation is sensitive to the choice of model and the parameters used in the analysis. Obviously, the model-independent analysis and spectral decomposition are desired for a solid discussion of the EDL structure. Our group measured the $\mathrm{Im}\chi^{(2)}$ spectra of the silica/water interface at pH 12.0 while systematically changing the salt (NaCl) concentration and demonstrated that the $\mathrm{Im}\chi^{(2)}$ spectra can be decomposed into two spectral components that are attributed to the SL and DL using simple spectral subtraction.[40] This study has led us to obtain molecular-level pictures of the EDL at the silica/water interface in a wide pH range based on spectral decomposition of the salt concentration-dependent $\mathrm{Im}\chi^{(2)}$ spectra.

The present study aims to obtain molecular insights into the silica/water interface at various pH (2.0−12.0), based on the $\mathrm{Im}\chi^{(2)}$ spectra in the OH stretch region measured at each pH with various salt concentrations (0.01 to 5.0 M). To realize model-independent spectral decomposition in the wide pH range, we use singular value decomposition (SVD) analysis. SVD is a mathematical method to find the number of independent spectral components, and it has widely been used for the analysis of various types of spectra.[44−46] The spectral decomposition based on SVD enables us to obtain clear molecular pictures of the water structures at the silica/water interface at various pHs, with the minimum assumption of the EDL model. It is found that the $\mathrm{Im}\chi^{(2)}$ spectra measured at various salt concentrations are decomposed into spectral components of water in SL and DL at all pHs. The pH dependence of the DL spectra enables us to estimate the surface charge density at each pH and pK_a value of the silica/water interface using the modified Gouy−Chapman (MGC) theory. Furthermore, the pH-dependent change of the SL spectrum allows us to clarify the change of the water structure in the vicinity of the silica surface, which is caused by the deprotonation/protonation of the silanol/silanolate groups.

2. METHODS

2.1. Materials. The silica substrates used in this study were fused silica windows with a diameter of 20 mm and thickness of 3 mm (IR grade, Pier optics). Before the experiments, each silica substrate was soaked in concentrated sulfuric acid (Nacalai Tesque, Inc., >99.5%) for at least 12 h to remove the organic contaminants. After being taken out of sulfuric acid, the silica substrate was washed with deionized water and cleaned by O_2 plasma for at least 10 min. Then, the silica substrate was half-coated with a 0.8 nm titanium buffer layer and 150 nm gold film using an electron beam evaporator (vide infra). Before HD-VSFG measurements, the silica substrate was cleaned again by O_2 plasma for at least 10 min before assembling it with the sample cell. The pH of each solution was adjusted by adding an adequate amount of HCl (Nacalai Tesque, Inc., 35% in H_2O) or NaOH (Nacalai Tesque, Inc., >99.5%) solutions into the solution. The salt-concentration dependence was examined using NaCl (Merck, 99.99%) as the salt. The pH values of the NaCl solutions were measured by a pH meter (Horiba LAQUAtwin pH-22) before and after HD-VSFG experiments.

The data discussed in the main text were obtained from a single silica window. The observed spectra somewhat depend on the silica windows used (see Section 3.2.2 and Supporting Information for the details). However, the essential arguments and conclusions are the same, free from this sample dependence.

2.2. HD-VSFG Measurements. We used an HD-VSFG setup that was newly constructed based on a diode-pumped Yb:KGW regenerative amplifier system (PHAROS SP-1.5, Light Conversion) operated at a repetition rate of 100 kHz. Its output (6 W) centered at ∼1030 nm was divided into two parts. One-third of the output (∼2 W) was used for generating narrowband NIR pulses (ω_1). After passing two bandpass filters, we obtained the ω_1 pulses with a center frequency of 1028.8 nm and a 25 cm^{-1} bandwidth in full width at half-maximum (FWHM). Two-third of the output (∼4 W) was directed into an optical parametric amplifier (OPA: ORPHEUS One, Light Conversion) to generate tunable IR pulses (ω_2). Since the FWHM of ω_2 was limited to ∼125 cm^{-1}, eight spectra were measured with different center ω_2 and merged to obtain the $\mathrm{Im}\chi^{(2)}$ spectra in the entire OH stretch region (2900−3800 cm^{-1}). The average power of the ω_2 beam was 40−80 mW, depending on the center ω_2 wavenumber.

The ω_1 and ω_2 pulses were first focused on a gold mirror to generate the SFG signal that was used as the local oscillator (LO)

https://doi.org/10.1021/jacs.2c11344
J. Am. Chem. Soc. 2023, 145, 8833−8846

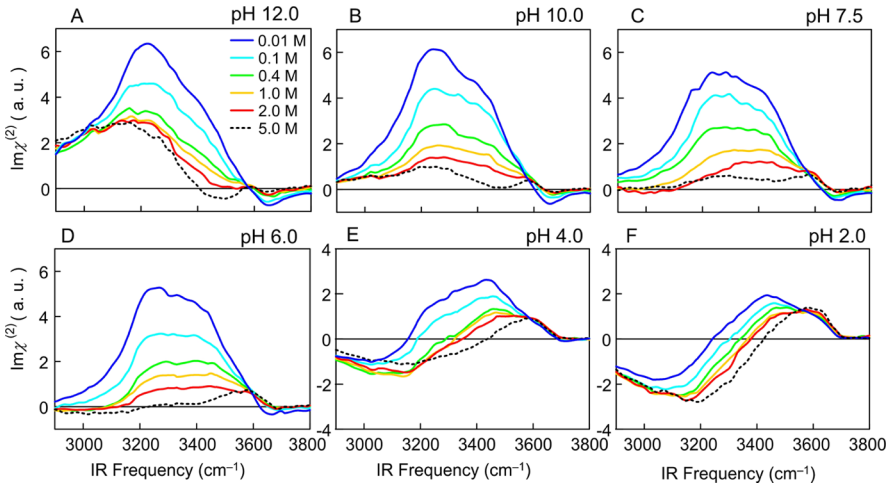

Figure 1. Im$\chi^{(2)}$ spectra of the silica/water interface with bulk NaCl concentrations from 0.01 to 5.0 M at various pH: (A) 12.0 ± 0.1, (B) 10.0 ± 0.1, (C) 7.5 ± 0.3, (D) 6.0 ± 0.2, (E) 4.0 ± 0.1, and (F) 2.0 ± 0.1. The Im$\chi^{(2)}$ spectra shown have been corrected by the complex conjugate of the reflectivity of LO and Fresnel factors at the silica/water interfaces.

SFG. (see Figure S1 for the optical configuration). Then, these three beams (ω_1, ω_2, and LO) were refocused to the buried silica/water interface by a concave mirror (r = 300 mm). A silica substrate was placed on top of a 1 mL aqueous solution in a Teflon cell. A 3 mm thick UV-grade silica plate was placed in the optical path of the LO before the sample cell to provide LO with a proper time delay. In addition, a 0.2 mm thick UV-grade silica plate was placed in the path of the ω_1 beam before the sample cell to compensate for the time delay between ω_1 and ω_2 caused by the sample silica substrate. The silica substrate was continuously moved in a range of y = ±0.2 mm horizontally (perpendicular to the incident plane of the ω_1 and ω_2 beams) during the measurements to avoid the accumulation of heat due to laser irradiation. The SFG signal generated at the silica/water interface and LO reflected at the silica/water interface were introduced into a polychromator (HRS-300-MS, Teledyne Princeton Instruments) and detected by a CCD (BLAZE-400HR-20, Teledyne Princeton Instruments). The SFG, ω_1, and ω_2 beams were s-, s-, and p-polarized, respectively (SSP polarization combination).

The raw spectra of the silica/water interface were normalized by the spectrum of the silica/Au film interface (used as "the temporary standard") that was obtained from the gold-coated half part of the sample silica substrate. The phase of the $\chi^{(2)}$ spectrum at this silica/Au film interface was calibrated using the $\chi^{(2)}$ spectra of the silica/air interface ("the true standard"), which was obtained from another half of the sample silica substrate with half-filled D_2O in the sample cell before introducing the solution for the measurement. The $\chi^{(2)}$ spectra shown in the present paper have been corrected for the complex conjugate of the reflectivity of LO and Fresnel factors at the silica/water interfaces, which vary with the salt concentration (see Section S2 in the Supporting Information for details).

3. RESULTS

3.1. Salt-Concentration-Dependent Im$\chi^{(2)}$ Spectra in a Wide pH Range and Spectral Decomposition. *3.1.1. Salt-Concentration-Dependent Im$\chi^{(2)}$ Spectra in the pH Range of pH 2.0−12.0.* Figure 1 shows the Im$\chi^{(2)}$ spectra of the silica/water interface at various pH measured with the NaCl concentration ranging from 0.01 to 5.0 M. As shown in Figure 1A, the Im$\chi^{(2)}$ spectra at pH 12.0 with diluted solutions (0.01 M) show a positive OH band peaked at ∼3200 cm^{-1} with a shoulder at ∼3450 cm^{-1} and a small negative OH band at 3650 cm^{-1}. The amplitude of the OH bands decreases gradually as the salt concentration increases from 0.01 to 5.0 M. As already discussed in previous studies,[24,47−49] this salt-induced decrease of the SFG signal is primarily attributed to the decrease of net orientation of the water molecules having "H-up" orientation (orienting H toward the silica surface) in DL. Although the phase of the SFG signal arising from DL is noticeably shifted at a very low NaCl concentration due to a large DL thickness, the phase shift is already not significant with a salt concentration at 0.01 M.[21,40,50] After the drastic amplitude decrease, the Im$\chi^{(2)}$ spectra show a positive band around ∼3150 cm^{-1}, a small negative band around ∼3500 cm^{-1}, and a small positive band around ∼3600 cm^{-1} at the high salt concentration of ≥2.0 M. These spectral changes observed at pH 12.0 are consistent with our previous report.[40]

Figure 1B−D shows the Im$\chi^{(2)}$ spectra at pH 10.0, pH 7.5, and pH 6.0. The observed salt-concentration-dependent Im$\chi^{(2)}$ spectra are similar to those observed at pH 12.0: the spectra show two positive OH bands peaked at ∼3200 and ∼3450 cm^{-1} with a small negative OH band at ∼3650 cm^{-1}, and the amplitudes of the positive 3200 and 3450 cm^{-1} bands decrease with the increases of the salt concentration. Nevertheless, several distinct features are recognized with the change in pH. First, in the dilute solutions, for example, 0.01 M, the relative amplitude of the 3200 cm^{-1} OH band to the 3450 cm^{-1} band decreases as the pH decreases. Second, in the spectra at high NaCl concentrations of ≥2.0 M, the amplitude of the positive signal below the 3150 cm^{-1} band drastically decreases with lowering pH, and it almost vanishes at pH 6.0. On the other hand, the amplitude of the positive signal around 3600 cm^{-1} increases.

Figure 1E,F shows Im$\chi^{(2)}$ spectra at pH 4.0 and 2.0, respectively. They show much smaller amplitudes and different spectral shapes compared to the spectra at higher pH. In the dilute solution (0.01 M), the Im$\chi^{(2)}$ spectra at pH 2.0 and 4.0 show one negative OH band at ∼3050 cm^{-1} and a broad positive OH band at ∼3450 cm^{-1}. These spectra accord well with the spectrum of the silica/water interface at pH 2.0 reported in our previous study.[39] The salt-induced spectral changes are also much smaller in magnitude at low pH than those observed at higher pH, although the amplitudes of the positive OH bands decrease in a similar way. In our previous study,[51] we assumed that EDL does not exist at pH 2.0 based on the prior zeta potential measurements. However, the salt concentration-dependent spectral change at pH 2.0 observed in this study clearly indicates the decrease of the "H-up" water

https://doi.org/10.1021/jacs.2c11344
J. Am. Chem. Soc. 2023, 145, 8833−8846

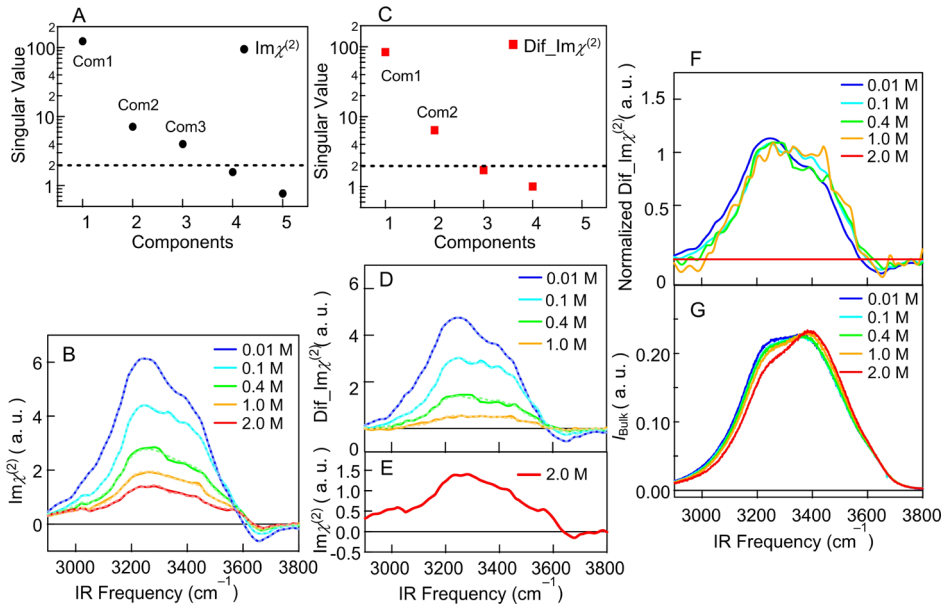

Figure 2. SVD analysis of the Im$\chi^{(2)}$ spectra at the silica/water interface. (A) Singular values obtained from the SVD analysis of the Im$\chi^{(2)}$ spectra at pH 10.0 ± 0.1. The dashed line is the indicator for <2% of the largest singular value, which can be regarded as noise. (B) Im$\chi^{(2)}$ spectra and the reconstructed Im$\chi^{(2)}$ spectra using three major components. (The reconstructed spectra are shown with broken lines.) (C) Singular values obtained from the SVD analysis of Dif_Im$\chi^{(2)}$ spectra (Im$\chi^{(2)}(C_0)$ − Im$\chi^{(2)}_{2.0M}$) at pH 10.0 ± 0.1. The dashed line is the indicator for <2% of the largest singular value, which can be regarded as noise. (D) Dif_Im$\chi^{(2)}$ spectra and reconstructed Dif_Im$\chi^{(2)}$ spectra using two major components. (The reconstructed spectra are shown with broken lines.) (E) Im$\chi^{(2)}$ spectra of the silica/water interface measured with 2.0 M NaCl. (F) The normalized Dif_Im$\chi^{(2)}$ spectra measured with different salt concentrations. (G) The bulk vibrational spectra ($I_{bulk} = \sqrt{I_{IR} \times I_{Raman}}$) of aqueous NaCl solutions measured with different NaCl concentrations.

signal from EDL water, indicating that negative charges still exist at the silica surface at pH 2.0.

In our previous study of the silica/water interface at pH 12.0,[40] we concluded that the Im$\chi^{(2)}$ spectral change up to 2.0 M NaCl is solely attributable to the decrease of the DL contribution due to the screening of the electric field by the counterion (Na^+), whereas the spectral change at higher salt concentrations (e.g., 5.0 M) arises from the salt-induced change of the SL. This conclusion was consistent with earlier conventional VSFG studies that concluded that the DL contribution is sufficiently suppressed with 2.0 M NaCl.[24,27,34,52] The Im$\chi^{(2)}$ spectra shown in Figure 1 indicate that this argument is valid for all pH examined in this study because the spectra measured with 5.0 M NaCl exhibit further changes in addition to the gradual spectral change observed up to 2.0 M. For instance, at pH 4.0 and 2.0, the spectral change between 1.0 and 2.0 M is already very small, but the difference between 2.0 and 5.0 M becomes substantial. This spectral change observed between 2.0 and 5.0 M cannot be explained by the decrease in the DL contribution. Therefore, we analyze and discuss the salt-concentration dependence of the Im$\chi^{(2)}$ spectra for the spectra measured with the NaCl concentration up to 2.0 M to avoid complications arising from too high salt concentration, such as the salt-induced change of SL, hereafter.

3.1.2. SVD Analysis and Separation of DL and SL Spectral Components. To obtain more quantitative information from the Im$\chi^{(2)}$ spectra, we performed SVD analysis for the salt concentration-dependent Im$\chi^{(2)}$ spectra measured at each pH. In this section, we describe the procedure and results of our analysis, using the Im$\chi^{(2)}$ spectra measured at pH 10.0 as an example. (See Section S3 in the Supporting Information for details of all the SVD analyses.)

Figure 2A shows the singular values obtained by the SVD analysis of the Im$\chi^{(2)}$ spectra at pH 10.0 (black dots). As seen, the singular values quickly become small, and only the first three values are significant. In fact, the spectra reconstructed using the first three components perfectly reproduce the experimental Im$\chi^{(2)}$ spectra at all the NaCl concentrations up to 2.0 M, as shown in Figure 2B (broken lines). We also calculated the Im$\chi^{(2)}$ spectra only with the first two components, but some deviation from the experimental spectra is noticeable, particularly at high NaCl concentrations at 2.0 M (Figure S5-2 in the Supporting Information). This result demonstrates that the salt concentration-dependent Im$\chi^{(2)}$ spectra at pH 10.0 can be represented by linear combinations of independent spectral components, and at least three spectral components are necessary to reproduce the spectra in a wide NaCl concentration range of 0.01−2.0 M.

With the increase of the NaCl concentration, the amplitude of the positive OH band monotonically decreases. This observation is explained by the shrinkage of the DL due to the screening of the electric field by the counterion Na^+. Since it is considered that the DL contribution is suppressed almost completely with 2.0 M NaCl, the decreased Im$\chi^{(2)}$ spectral component is attributable to the spectrum in DL (Im$\chi^{(2)}_{DL}$), whereas the Im$\chi^{(2)}$ spectrum measured at 2.0 M NaCl is considered to be the spectrum of SL (Im$\chi^{(2)}_{SL,2.0M}$) at 2.0 M NaCl, although Im$\chi^{(2)}_{2.0M}$ might still contain a very small amount of the DL contribution.

We subtract the Im$\chi^{(2)}_{2.0M}$ spectrum from the Im$\chi^{(2)}$ spectra measured with various NaCl concentrations (Dif_Im$\chi^{(2)}$ = Im$\chi^{(2)}$ − Im$\chi^{(2)}_{2.0M}$). The obtained Dif_Im$\chi^{(2)}$ spectra at pH 10.0 are shown in Figure 2D. These spectra show two OH bands peaked at 3200 and 3450 cm^{-1}, and the amplitudes of these two bands decrease with increasing the NaCl concentration.

https://doi.org/10.1021/jacs.2c11344
J. Am. Chem. Soc. 2023, 145, 8833−8846

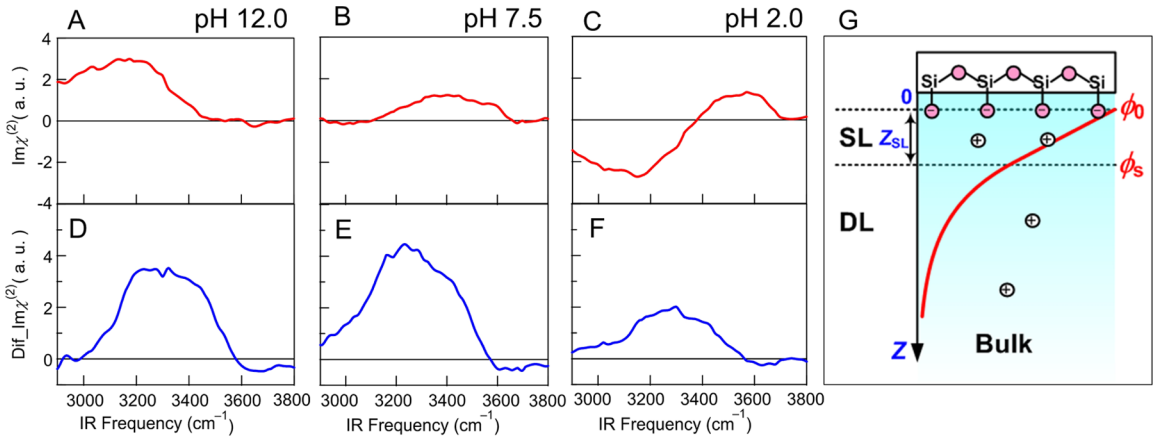

Figure 3. Separated SL spectra and DL spectra at the silica/water interface and the Stern model of EDL. SL spectra at pH 12.0 (A), 7.5 (B), and 2.0 (C); DL spectra with 0.01 M NaCl solution at pH 12.0 (D), 7.5 (E), and 2.0 (F). (G) Scheme of the Stern model of the EDL structure. SL: compact Stern layer; DL: diffuse Gouy−Chapman layer; Z_{SL}: thickness of the Stern layer; ϕ_0: potential at the silica surface (surface potential); ϕ_S: potential at the edge of the Stern layer (Stern potential).

We also performed the SVD analysis of the Dif_Im$\chi^{(2)}$ and found that the third singular value becomes negligibly small (Figure 2C), implying that the Dif_Im$\chi^{(2)}$ spectra can be reproduced only with two spectral components (the broken lines in Figure 2D). We also calculated the Dif_Im$\chi^{(2)}$ spectra only with the first component, but some deviations from the experimental spectra are noticeable (Figure S6-2 in the Supporting Information). This result indicates that the subtraction of the Im$\chi^{(2)}_{2.0M}$ spectrum removes one spectral component from the Im$\chi^{(2)}$ spectra. Since the Im$\chi^{(2)}_{2.0M}$ spectrum can be regarded as the SL spectrum at 2.0 M (Im$\chi^{(2)}_{2.0M}$ ≈ Im$\chi^{(2)}_{SL,2.0M}$), this means that the component identical to the SL spectrum at 2.0 M (Im$\chi^{(2)}_{SL,2.0M}$) commonly exists unchanged in all the Im$\chi^{(2)}$ spectra measured with different NaCl concentrations.

The Dif_Im$\chi^{(2)}$ spectra, which are obtained with the subtraction of the Im$\chi^{(2)}_{2.0M}$ spectrum, are shown in Figure 2F after amplitude normalization at 3300 cm^{-1}. The SVD analysis indicates that there are two spectral components in the Dif_Im$\chi^{(2)}$ spectra. The origin of one component is obvious, that is, the DL water spectrum. The question is the origin of the second spectral component. To clarify it, we estimate the corresponding bulk water spectra with the square root of the product of the IR and Raman spectra of bulk water, that is, $I_{bulk} = \sqrt{I_{IR} \times I_{Raman}}$, because the VSFG optical process can be decomposed into the IR and Raman transitions. The calculated I_{bulk} spectra are shown in Figure 2G, and the original IR and Raman spectra are given in Figure S7-1 in the Supporting Information. The salt concentration-dependent Dif_Im$\chi^{(2)}$ spectra (Figure 2F) and the I_{bulk} spectra (Figure 2G) exhibit very similar spectral changes: the amplitude of the 3200 cm^{-1} band relative to the 3450 cm^{-1} band gradually decreases as the NaCl concentration increases from 0.01 to 2.0 M. In fact, the SVD analysis shows that the I_{bulk} spectra are reproduced with two independent spectral components, as in the case of Dif_Im$\chi^{(2)}$ (see Section S4 in the Supporting Information for the details). Since it is known that the spectra of the water in DL are similar to the spectra of bulk water,[40,41,43] this similarity strongly indicates that the second component of the Dif_Im$\chi^{(2)}$ spectra is the component required to reproduce the salt-induced change of the DL water spectrum. In other words, the Dif_Im$\chi^{(2)}$ spectra are solely attributed to the DL water spectra, which exhibit significant amplitude decrease accompanied with a slight spectral change with the increase of the salt concentration. This result also implies that the SL spectrum at 2.0 M (Im$\chi^{(2)}_{2.0M}$ ≈ Im$\chi^{(2)}_{SL,2.0M}$) exists as the unchanged spectra of SL (Im$\chi^{(2)}_{SL}$) in all Im$\chi^{(2)}$ spectra in the salt concentration range from 0.01 to 2.0 M. It means that, surprisingly, the SL formed at low NaCl concentration (0.01 M) is unchanged up to the salt concentration as high as 2.0 M.

The analysis using SVD clarifies that we can decompose salt-concentration-dependent Im$\chi^{(2)}$ spectra at pH 10.0 into two spectral components: (1) the spectrum of the water in DL (Im$\chi^{(2)}_{DL}$) that exhibits NaCl-concentration-dependent spectral change and becomes smaller and finally negligible with the addition of NaCl, and (2) the spectrum of the water in SL (Im$\chi^{(2)}_{SL}$) that exists in all the Im$\chi^{(2)}$ spectra and unchanged with the change in NaCl concentration from 0.01 to 2.0 M.

3.1.3. Separated DL and SL Spectra at Different pH Values. We perform SVD analysis for the salt concentration-dependent Im$\chi^{(2)}$ spectra measured at all pH from 2.0 to 12.0 and found that the spectra at other pH can also be analyzed in the same way as the case of pH 10.0 (see Figures S4−S6, and S7-3 in the Supporting Information): at each pH, the Im$\chi^{(2)}_{2.0M}$ spectrum can be considered to be the unchanged Im$\chi^{(2)}_{SL}$ spectrum that is included in all the spectra measured with NaCl concentrations from 0.01 to 2.0 M, whereas Dif_Im$\chi^{(2)}$ spectra are attributed to the Im$\chi^{(2)}_{DL}$ spectra that exhibit spectra similar to the corresponding bulk water spectra. This means that the Im$\chi^{(2)}$ spectra at all pHs examined (pH 2.0−12.0) are represented as the sum of the Im$\chi^{(2)}_{SL}$ and Im$\chi^{(2)}_{DL}$ spectra

$$\mathrm{Im}\chi^{(2)} = \mathrm{Im}\chi^{(2)}_{SL} + \mathrm{Im}\chi^{(2)}_{DL} \quad (1)$$

We stress that formula 1 is derived from the model-free spectral decomposition of the Im$\chi^{(2)}$ spectra using the SVD without assumption of the Stern model. In other words, the present HD-VSFG study provides direct spectroscopic evidence that the EDL structure at the silica/water interface is well described by the Stern model in a wide pH range from 2.0 to 12.0. The separated Im$\chi^{(2)}_{DL}$ spectra and Im$\chi^{(2)}_{SL}$ spectra at pH 12.0, pH 7.5, and pH 2.0 are shown in Figure 3, along with the schematic of the Stern model of EDL.

https://doi.org/10.1021/jacs.2c11344
J. Am. Chem. Soc. 2023, 145, 8833−8846

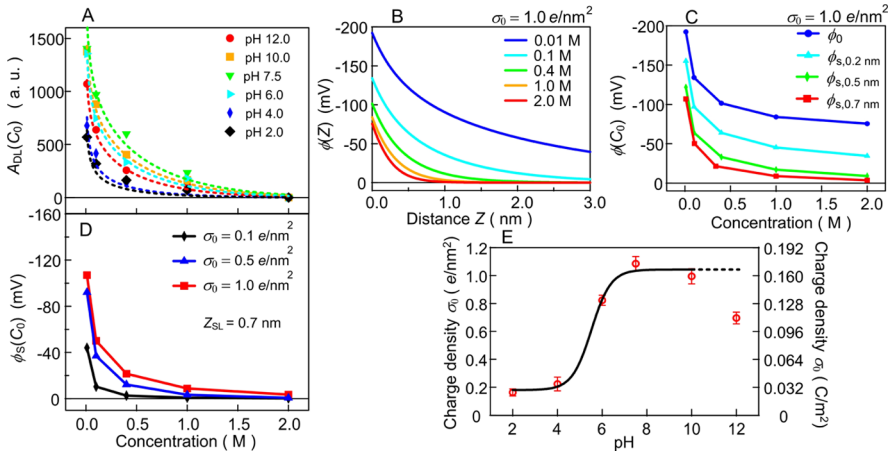

Figure 4. Analysis of the Im$\chi^{(2)}$ signal from the diffuse Gouy−Chapman layer (DL) at the silica/water interface. (A) NaCl-concentration dependence of $A_{DL}(C_0)$ at different pH. The dashed lines are the best fits using Z_{SL} = 0.7 nm. (B) Distance dependence of the potential $\phi(Z)$ calculated by the MGC theory for the surface charge density of σ_0 = 1.0 e/nm^2 = 0.16 C/m^2. (C) Salt-concentration dependence of the surface potential ϕ_0 and the Stern potential ϕ_S (Z_{SL} = 0.2, 0.5, and 0.7 nm) calculated by the MGC theory. (D) Salt-concentration dependence of the Stern potential ϕ_S calculated by the MGC theory for the surface charge density of σ_0 = 0.1, 0.5, and 1.0 e/nm^2 (corresponds to 0.016, 0.08, and 0.16 C/m^2, respectively). (E) pH dependence of the surface charge density σ_0 estimated from the experimental Im$\chi^{(2)}_{DL}$ spectra. The black solid line is the best fit to eq 5 for the range between pH 2.0 and pH 10.0. The dashed black line is extended from the solid black line for an eye guide.

As shown in Figure 3A−C, the Im$\chi^{(2)}_{SL}$ spectra significantly change as pH changes. This reveals that the water structure in the Stern layer substantially changes with pH, reflecting the change of the negative charge density due to the protonation/deprotonation at the silica surface. In contrast, as shown in Figure 3D−F, the Im$\chi^{(2)}_{DL}$ spectra exhibit similar positive OH bands centered at ∼3300 cm^{-1}. They are assigned to bulk-like water molecules having H-up orientation (toward the silica surface) in DL, which is induced by the electric field due to the negative charge at the silica surface.[40,41,43] Observation of the H-up water in DL at all pH directly indicates that the silica surface is negatively charged in the pH range of pH 2.0−12.0. The amplitude of the Im$\chi^{(2)}_{DL}$ spectra does not show a significant change when pH changes from 12.0 to 7.5, whereas it decreases to about half from pH 7.5 to 2.0. It indicates that the negative charge, and hence the protonation state of the silica surface, substantially changes in this pH region (vide infra).

In the following sections, we separately analyze the pH-dependent changes of the Im$\chi^{(2)}_{DL}$ and Im$\chi^{(2)}_{SL}$ spectra to evaluate the pK_a value of the silica surface and pH-dependent water structure in the Stern layer, respectively.

3.2. Analysis of DL Spectra and the pK_a Value of the Silica Surface.

In this section, we analyze the DL spectra (Im$\chi^{(2)}_{DL}$ = Dif_Im$\chi^{(2)}$) to estimate the charge density σ_0 at different pHs and the pK_a value of the protonation/deprotonation equilibrium of the silica surface.

3.2.1. Estimation of Surface Charge Density. The amplitude of Im$\chi^{(2)}_{DL}$ represents the amount of the oriented water in DL, which is determined by the electric field due to the negative charge at the silica surface. To estimate the charge density σ_0 at the silica surface from the Im$\chi^{(2)}$ spectra, we first evaluate the Im$\chi^{(2)}_{DL}$ amplitude at a NaCl concentration C_0 by integrating the Dif_Im$\chi^{(2)}$ spectra in the frequency range of 2900−3800 cm^{-1}

$$A_{DL}(C_0) = \int_{2900\mathrm{cm}^{-1}}^{3800\mathrm{cm}^{-1}} \left|\mathrm{Im}\chi^{(2)}(C_0) - \mathrm{Im}\chi^{(2)}_{2.0\mathrm{M}}\right| \mathrm{d}\omega = \int_{2900\mathrm{cm}^{-1}}^{3800\mathrm{cm}^{-1}} \left|\mathrm{Im}\chi^{(2)}_{DL}(C_0)\right| \mathrm{d}\omega \quad (2)$$

Then, we use $A_{DL}(C_0)$ as a measure of the magnitude of the spectral response from DL. Figure 4A shows $A_{DL}(C_0)$ calculated for the NaCl concentration of 0.01−2.0 M at different pHs. As seen in this figure, $A_{DL}(C_0)$ decreases as the NaCl concentration increases, reflecting the shrinkage of DL. It is known that the amplitude of the spectral response from DL is proportional to the integration of the electric field ($E(Z)$ = −dϕ/dZ) over the DL[9,23,40,53]

$$\chi^{(2)}_{DL} = \int_{Z_{SL}}^{\infty} -e^{i\Delta k_Z Z} \frac{d\phi}{dZ} \chi^{(2)}_{DL,N} dZ = \phi_S \chi^{(2)}_{DL,N} \quad (3)$$

Here, Z_{SL} is the thickness of the Stern layer, ϕ_S is the Stern potential (the potential at the border between SL and DL), Δk_Z is the inverse of coherence length,[23,53,54] Z is the distance from the silica surface, and $\chi^{(2)}_{DL,N}$ is the $\chi^{(2)}_{DL}$ amplitude per unit ϕ_S. This $\chi^{(2)}_{DL,N}$ is often represented as $\chi^{(3)}_B$ and is treated as "third-order" nonlinear susceptibility[9,21,24,25,48] because this component arises under the existence of three electric fields, that is, the electric fields of incident ω_1 and ω_2 light, and a static electric field generated by the surface charge. Nevertheless, it was recently shown theoretically that the VSFG signal from DL predominantly arises from the second-order optical process, originating from hyperpolarizability (β_{ijk}), and that the role of the static electric field is to make water molecules oriented in DL.[41,49] To emphasize this point, we represent this spectral component as $\chi^{(2)}_{DL,N}$ in this paper, although it is equivalent to $\chi^{(3)}_B$ that arises from the orientation of the molecules. Note that the most right-hand side expression of formula 3 is obtained by neglecting $e^{i\Delta k_Z Z}$ in DL, which is valid for the $C_0 \geq$ 0.01 M used in this study.[23,53,54]

It is worth mentioning that formula 3 is slightly different from the formula in the literature:[9,21,55] The integration along

https://doi.org/10.1021/jacs.2c11344
J. Am. Chem. Soc. 2023, 145, 8833−8846

the Z axis starts not from 0 (or 0+) but Z_{SL}, and $\mathrm{Im}\chi^{(2)}_{DL}$ is proportional not to the surface potential ϕ_0 but to the Stern potential ϕ_S. By using ϕ_S, formula 3 can adequately treat the Stern layer as a layer having a finite thickness, being consistent with the Stern model. The difference between ϕ_0 and ϕ_S is the potential decrease in the Stern layer. (Similar treatments can also be found in recent literature.[43,56,57]) Formula 3 is equivalent to the following formula that we can use for analyzing the $\mathrm{Im}\chi^{(2)}_{DL}$ spectra measured in this study

$$A_{DL}(C_0) = \phi_S(C_0)\cdot A_{DL,N} \tag{4}$$

where $A_{DL,N}$ is the A_{DL} at the unit ϕ_S. The formula 4 enables us to estimate the salt-concentration dependence of the Stern potential ϕ_S from the $\mathrm{Im}\chi^{(2)}_{DL}$ spectral amplitudes obtained experimentally.

We use the modified GC (MGC) theory to relate ϕ_S with the surface potential ϕ_0 and surface charge density σ_0 (see Section S5 in the Supporting Information for the details). As an example, Figure 4B depicts the distance dependence of the potential, $\phi(Z)$, which is calculated with the MGC theory for σ_0 = 1.0 e/nm^2. In this calculation, we assume that hydrated ions have an ionic diameter (a) of 0.7 nm, according to the previous studies.[23,40] As shown in this figure, the potential $\phi(Z)$ in the EDL of a 0.01 M NaCl solution decreases from −192 to −40 mV as the distance Z increases from 0 to 3.0 nm. Furthermore, as the NaCl concentration increases from 0.01 to 2.0 M, $\phi(Z)$ exhibits more and more sharp drops as Z increases due to the screening effect of the counterion. At all the NaCl concentrations, however, $\phi(Z)$ exhibits the largest decrease in the distance range of Z = 0−0.7 nm. The magnitude of this large potential decrease in the vicinity of the silica surface is insensitive to the NaCl concentration.

The salt-concentration dependence of the surface potential $\phi_0 = \phi(Z = 0\ \mathrm{nm})$ calculated with the MGC theory is plotted in Figure 4C (blue line). The calculated ϕ_0 decreases as the NaCl concentration increases. However, it does not approach zero even at a NaCl concentration as high as 2.0 M and exhibits an offset. This offset potential comes from the potential drop within the Stern layer, that is, $\phi_0 - \phi_S$, which remains even when the electric field in DL is completely suppressed by the screening effect of the highly concentrated counterions. In other words, we can calculate the Stern potential ϕ_S by subtracting this offset from the surface potential ϕ_0. We calculated the Stern potential $\phi_S = \phi(Z = Z_{SL})$ by assuming several thicknesses of SL (Z_{SL}) and found that ϕ_S shows no offset when we set Z_{SL} at 0.7 nm (Figure 4C, red line). Therefore, we can obtain ϕ_S from ϕ_0 by subtracting the $\phi_0 - \phi_S = \int_0^{Z_{SL}} \left(-\frac{d\phi(Z)}{dZ}\right) dZ$ value using Z_{SL} = 0.7 nm.

The salt-concentration dependence of $\phi_S(C_0)$ is calculated for different σ_0 values and shown in Figure 4D. As we can expect from formula 4, the calculated $\phi_S(C_0)$ curves show excellent similarity to the $A_{DL}(C_0)$ curves that are experimentally obtained at each pH (Figure 4A). This agreement assures that the MGC theory adequately describes the NaCl-concentration dependence of $\mathrm{Im}\chi^{(2)}_{DL}$ from 0.01 to 2.0 M and that the Z_{SL} value we adopted is adequate. The calculated $\phi_S(C_0)$ curves change with the change of the σ_0 value used, whereas the experimental $A_{DL}(C_0)$ curves change with the change of pH. It means that we can estimate the surface charge density σ_0 at each pH by searching for the σ_0 value that can best reproduce the $A_{DL}(C_0)$ curve determined experimentally. The σ_0 values at different pHs estimated in this way are plotted in Figure 4E, and the best fits to the $A_{DL}(C_0)$ curves are shown in Figure 4A (broken lines).

3.2.2. Estimation of the Silica Surface pK_a Value. The estimated σ_0 values directly reflect the surface density of the SiO^- group because the SiO^- group is the only source of the negative charge at the silica surface. As seen in Figure 4E, the pH dependence of the σ_0 value exhibits a significant increase only in the pH region between pH 4.0 and 6.0, implying that the SiO^- density substantially increases in this pH region. In other words, the $\mathrm{Im}\chi^{(2)}_{DL}$ spectra obtained in this study indicate a single pK_a value for the deprotonation of the SiOH site at the silica/water interface. The pH dependence of σ_0 can be represented by the following equation based on the SiO^-/SiOH equilibrium[58]

$$\sigma_0(\mathrm{pH}) = \frac{D_M}{1 + 10^{\mathrm{p}K_a}[H^+]_s} e + D_0,$$
$$[H^+]_s = 10^{-\mathrm{pH}} \exp\left(-\frac{e\phi_0}{k_b T}\right) \tag{5}$$

Here, $[H^+]_s$ is the H^+ concentration at the interface, D_M is the site density of the SiOH groups (which are deprotonated by the pH titration), e is the elemental charge, and D_0 is the density of the negatively charged SiO^- site at pH 2.0. Figure 4E also shows that the σ_0 value estimated at pH 12.0 is substantially smaller than the value estimated at pH 10.0, which cannot be explained simply with the SiO^-/SiOH equilibrium because it is very unlikely that the SiO^- site is more protonated at the higher pH. (This deviation will be discussed in Section 4.2.) Therefore, a fitting of the σ_0 values with formula 5 is made only for the pH range of pH 2.0−10.0, and pK_a = 4.8 ± 0.2 is obtained. (The best fit is shown in Figure 4E with the black solid line). We also collected the $\mathrm{Im}\chi^{(2)}_{DL}$ spectra at the silica/water interface using different silica substrates (Figure S9A in the Supporting Information). It was found that the obtained spectra somewhat deviated, indicating that the SiO^-/SiOH site density (and hence the surface charge density σ_0) is substantially dependent on substrate. However, the pH dependence of the $\mathrm{Im}\chi^{(2)}_{DL}$ amplitude exhibits a significant change only in a single, similar pH range, regardless of the difference in the substrates. This indicates that each silica substrate has only a single pK_a value in the pH range examined in this study, although the SiO^-/SiOH site density is noticeably varied.[59−61]

3.3. Analysis of SL Spectra and pH-Dependent SL Water Structure. In this section, we analyze the SL spectra ($\mathrm{Im}\chi^{(2)}_{SL}$) obtained at different pHs to elucidate the SL water structure and its change with the change of pH. We apply SVD analysis to the pH-dependent $\mathrm{Im}\chi^{(2)}_{SL}$ spectra and obtain a molecular-level picture of the water structure in SL that changes with the change of the charge density at the silica surface.

3.3.1. SL Spectra at Different pH and Spectral Decomposition. Figure 5A shows $\mathrm{Im}\chi^{(2)}$ spectra of SL ($\mathrm{Im}\chi^{(2)}_{SL}$:$\mathrm{Im}\chi^{(2)}$ spectra with 2.0 M NaCl) at the silica/water interface obtained in the pH range of 2.0−12.0. As shown, the $\mathrm{Im}\chi^{(2)}_{SL}$ spectrum drastically changes with the change of pH: At pH 12.0, the spectrum shows a positive broad band peaked at ∼3200 cm^{-1}.

https://doi.org/10.1021/jacs.2c11344
J. Am. Chem. Soc. 2023, 145, 8833−8846

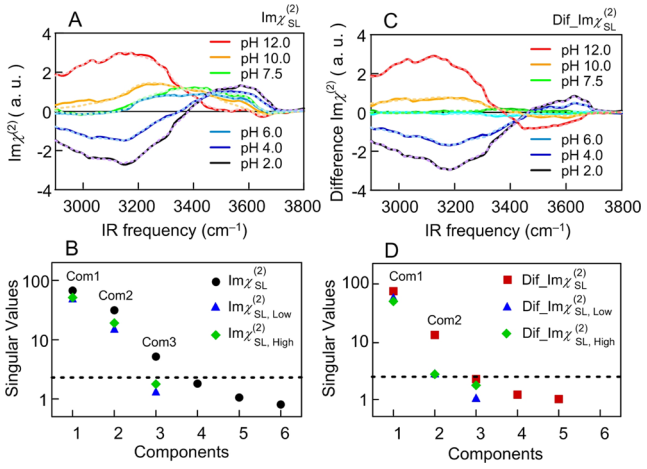

Figure 5. SVD analysis of the Im$\chi^{(2)}$ spectra from the compact Stern layer (SL) at the silica/water interface. (A) SL water spectra ($\mathrm{Im}\chi^{(2)}_{SL}$ = $\mathrm{Im}\chi^{(2)}_{2.0M}$) at various pH. The reconstructed spectra are also shown with broken lines. (B) Singular values obtained by the SVD analysis of the $\mathrm{Im}\chi^{(2)}_{SL}$ spectra. $\mathrm{Im}\chi^{(2)}_{SL,low}$ represents the $\mathrm{Im}\chi^{(2)}_{SL}$ spectra in the low pH region (pH 6.0, 4.0, and 2.0). $\mathrm{Im}\chi^{(2)}_{SL,high}$ represents the $\mathrm{Im}\chi^{(2)}_{SL}$ spectra in the high pH region (pH 12.0, pH 10.0, and pH 7.5). The dashed line is the indicator for <2% of the largest singular value, which can be regarded as noise. (C) Difference $\mathrm{Im}\chi^{(2)}_{SL}$ spectra ($\mathrm{Dif\_Im}\chi^{(2)}_{SL}$) at various pH. The reconstructed spectra are also shown with broken lines. (D) Singular values obtained by the SVD analysis of $\mathrm{Dif\_Im}\chi^{(2)}_{SL}$. $\mathrm{Dif\_Im}\chi^{(2)}_{SL,low}$ represents the $\mathrm{Dif\_Im}\chi^{(2)}_{SL}$ spectra in the low pH region (pH 6.0, 4.0, and 2.0). $\mathrm{Dif\_Im}\chi^{(2)}_{SL,high}$ represents the $\mathrm{Dif\_Im}\chi^{(2)}_{SL}$ spectra in the high pH region (pH 12.0, 10.0, and 7.5). The dashed line is the indicator for <2% of the largest singular value, which can be regarded as noise.

As pH lowers to pH 6.0, the amplitude of the positive band decreases while exhibiting a redshift. At the low pH of pH 4.0 and 2.0, a negative OH band peaked at ~3150 cm^{-1} appears in the low-frequency region, and a positive band appears at ~3550 cm^{-1} in the high-frequency region. The amplitudes of these positive and negative OH bands increase as the pH decreases from pH 4.0 to 2.0.

To elucidate the molecular origin of the above-described spectral change, we performed the SVD analysis of the pH-dependent $\mathrm{Im}\chi^{(2)}_{SL}$ and obtained singular values (Figure 5B). The analysis shows three significant singular values. The spectra reconstructed with the three major singular values reproduce $\mathrm{Im}\chi^{(2)}_{SL}$ spectra very well in the pH range of pH 2.0−12.0 (broken lines in Figure 5A), indicating that the pH-dependent $\mathrm{Im}\chi^{(2)}_{SL}$ spectra can be represented as the sum of three independent spectral components. We also perform the SVD analysis of the $\mathrm{Im}\chi^{(2)}_{SL}$ spectra in the high pH region (pH 7.5−pH 12.0; $\mathrm{Im}\chi^{(2)}_{SL,high}$) and low pH region (pH 2.0−pH 6.0; $\mathrm{Im}\chi^{(2)}_{SL,low}$) separately, and found that they have only two significant components (Figure 5B). This result implies that the $\mathrm{Im}\chi^{(2)}_{SL,high}$ and $\mathrm{Im}\chi^{(2)}_{SL,low}$ spectra contain two spectral components, but one of them does not appear in the other. Furthermore, the $\mathrm{Im}\chi^{(2)}_{SL}$ spectra in the neutral pH region (pH 6.0 and pH 7.5; $\mathrm{Im}\chi^{(2)}_{SL,neutral}$) exhibit a completely different spectral feature from $\mathrm{Im}\chi^{(2)}_{SL}$ at the high and low pH regions. Thus, we can consider that the $\mathrm{Im}\chi^{(2)}_{SL,neutral}$ is the component that is present in all pH-dependent $\mathrm{Im}\chi^{(2)}_{SL}$ spectra and that the $\mathrm{Im}\chi^{(2)}_{SL,high}$ and $\mathrm{Im}\chi^{(2)}_{SL,low}$ spectra are the sum of the $\mathrm{Im}\chi^{(2)}_{SL,neutral}$ and another spectral component. To verify this idea, the difference $\mathrm{Im}\chi^{(2)}_{SL}$ spectra ($\mathrm{Dif\_Im}\chi^{(2)}_{SL}$) are calculated by subtracting $\mathrm{Im}\chi^{(2)}_{SL,neutral}$ from the $\mathrm{Im}\chi^{(2)}_{SL}$ spectra at each pH

$$\mathrm{Dif\_Im}\chi^{(2)}_{SL} = \mathrm{Im}\chi^{(2)}_{SL} - \mathrm{Im}\chi^{(2)}_{SL,neutral},$$
$$\mathrm{Im}\chi^{(2)}_{SL,neutral} \equiv (\mathrm{Im}\chi^{(2)}_{SL,pH6.0} + \mathrm{Im}\chi^{(2)}_{SL,pH7.5})/2 \quad (6)$$

Here, we adopt the average of the $\mathrm{Im}\chi^{(2)}_{SL}$ spectra at pH 6.0 and 7.5 as $\mathrm{Im}\chi^{(2)}_{SL,neutral}$. The calculated $\mathrm{Dif\_Im}\chi^{(2)}_{SL}$ spectra are shown in Figure 5C. As expected, the SVD analysis of $\mathrm{Dif\_Im}\chi^{(2)}_{SL}$ spectra in all pH ranges from pH 2.0 to 12.0 only show two

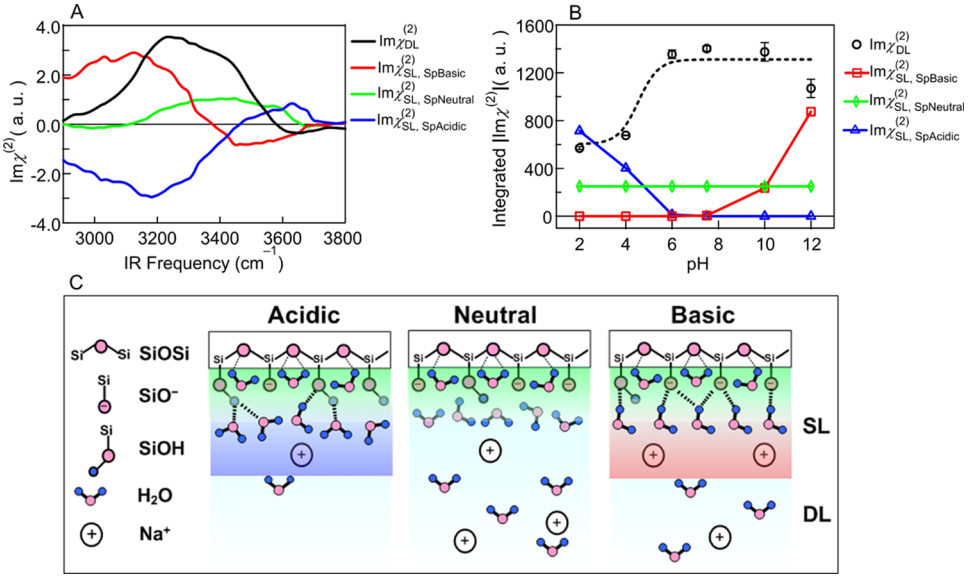

Figure 6. Spectral components of the Im$\chi^{(2)}$ spectra at the silica/water interface in a pH range from 2.0 to 12.0. (A) Spectra of four spectral components in the Im$\chi^{(2)}$ spectra ($\mathrm{Im}\chi^{(2)}_{DL}$, $\mathrm{Im}\chi^{(2)}_{SL,SpBasic}$, $\mathrm{Im}\chi^{(2)}_{SL,SpNeutral}$, and $\mathrm{Im}\chi^{(2)}_{SL,SpAcidic}$.) The spectra of the $\mathrm{Im}\chi^{(2)}_{DL}$ component were calculated by averaging the $\mathrm{Im}\chi^{(2)}_{DL}$ spectra measured with 0.01 M NaCl at pH 2.0−12.0. (B) pH-dependence of the integrated amplitude of each spectral component. The broken line is an eye guide. (C) Schematic of pH-dependent water structure at the silica/water interface. SL: compact Stern layer; DL: diffuse Gouy−Chapman layer.

https://doi.org/10.1021/jacs.2c11344
J. Am. Chem. Soc. 2023, 145, 8833−8846

significant singular values, as shown with red squares in Figure 5D. (The Dif_Im$\chi^{(2)}_{SL}$ spectra reconstructed with the two components are also shown in Figure 5B with broken lines.) This reduction of the significant singular values for Dif_Im$\chi^{(2)}_{SL}$ implies that the subtraction of Im$\chi^{(2)}_{SL,neutral}$ erases the third spectral component. In other words, the Im$\chi^{(2)}_{SL,neutral}$ is the constant/unchanged component that is present in the Im$\chi^{(2)}_{SL}$ spectra at all pHs.

As shown in Figure 5C, the spectral feature of the Dif_Im$\chi^{(2)}_{SL}$ at high pH (pH 12.0 and pH 10.0) is very similar to each other, while that at low pH (pH 4.0 and pH 2.0) is also very similar to each other. This similarity can be more readily seen after amplitude normalization (Figure S10). In fact, the SVD analyses of the Dif_Im$\chi^{(2)}_{SL}$ spectra at the low pH (Dif_Im$\chi^{(2)}_{SL,low}$) and the high pH (Dif_Im$\chi^{(2)}_{SL,high}$) show only a single significant singular value, indicating that each of Dif_Im$\chi^{(2)}_{SL,high}$ and Dif_Im$\chi^{(2)}_{SL,low}$ contain, essentially, only a single spectral component. Therefore, these spectral components have clear physical meanings: Im$\chi^{(2)}_{SL}$ spectra specific to the high and low pH regions, which we name Im$\chi^{(2)}_{SL,SpBasic}$ and Im$\chi^{(2)}_{SL,SpAcidic}$, respectively.

Consequently, the SVD analysis reveals that the Im$\chi^{(2)}_{SL}$ spectra in the pH range of pH 2.0−12.0 can be separated into the following three spectral components: the spectral component that appears only at high pH (Im$\chi^{(2)}_{SL,SpBasic}$), the spectral component that appears only at low pH (Im$\chi^{(2)}_{SL,SpAcidic}$), and the spectral component that appears at all pH without change (Im$\chi^{(2)}_{SL,SpNeutral}$).

3.3.2. pH-Dependent Water Structure in SL. The spectra of the three spectral components in the Im$\chi^{(2)}$ spectra of SL (Im$\chi^{(2)}_{SL,SpBasic}$, Im$\chi^{(2)}_{SL,SpNeutral}$, and Im$\chi^{(2)}_{SL,SpAcidic}$) are shown in Figure 6A. They represent different water species that appear at different pH in SL of the silica/water interface. In this figure, the Im$\chi^{(2)}$ spectra of DL (Im$\chi^{(2)}_{DL}$) are also shown for comparison, which is calculated by averaging the Im$\chi^{(2)}_{DL}$ spectra measured with 0.01 M NaCl at pH 2.0−12.0. The Im$\chi^{(2)}_{SL,SpBasic}$ spectrum (red line in Figure 6A), which appears only at high pH, shows a major positive OH band peaked at ∼3150 cm^{-1} and a smaller negative OH band around 3500 cm^{-1}. The low-frequency positive OH band indicates H-up (orienting H toward the silica surface) OH groups that are strongly hydrogen-bonded. The negative OH band in the intermediate frequency region indicates the presence of H-down (orienting H away from the silica surface) OH groups that are hydrogen-bonded with medium strength. The absence of the isotopic dilution effect in the Im$\chi^{(2)}_{SL}$ spectrum at pH 12.0 reported in our previous paper indicates that the spectrum at high pH mainly arises from water molecules that are asymmetrically hydrogen bonded.[40] Therefore, the Im$\chi^{(2)}_{SL,SpBasic}$ spectrum is attributed to the water molecule, which has an OH group that is strongly hydrogen-bonded to the SiO$^-$ groups at the silica surface with H-up orientation and has another OH group that is hydrogen-bonded to other neighboring water molecules with H-down orientation. This picture is consistent with the water structure in SL at the high pH proposed in our previous paper.[40]

The Im$\chi^{(2)}_{SL,SpNeutral}$ spectrum (green line in Figure 6A) shows a broad positive OH band peaked at ∼3400 cm^{-1}. This component appears at all pH range from pH 2.0 to 12.0 with a constant amplitude. The positive sign of this band indicates that the corresponding OH group has the H-up orientation by the interaction with the silica surface. The Si−O−Si bridge site is present at the silica surface, irrespective of the difference in pH as well as deprotonation/protonation of the SiOH/SiO$^-$ site, and its O atom can interact with the OH of water molecules with hydrogen bonding. In our previous HD-VSFG study on the silica/water interface at pH 12.0, we assigned a small positive band at 3600 cm^{-1} to the water OH interacting with the Si−O−Si bridge site.[40] However, the rigorous SVD analysis in this study shows that the small spectral feature at ∼3600 cm^{-1} appears as a result of overlap with the Im$\chi^{(2)}_{SL,SpBasic}$ spectral component and that the true spectrum due to the OH group interacting with the Si−O−Si bridge site exhibits a much broader positive band. Nevertheless, this water species is considered minor in SL at the silica/water interface because the amplitude of the Im$\chi^{(2)}_{SL,SpNeutral}$ spectrum is small compared to the other two spectral components.

The Im$\chi^{(2)}_{SL,SpAcidic}$ spectrum (blue line in Figure 6A), which appears only at low pH, shows a major negative OH band peaked at ∼3200 cm^{-1} and a smaller positive OH band peaked at ∼3650 cm^{-1}. The low-frequency negative OH band indicates strongly hydrogen-bonded OH groups with H-down orientation. The peak frequency of this negative OH band is slightly higher than the frequency of the positive OH band in the Im$\chi^{(2)}_{SL,SpBasic}$ that is assigned to the OH group interacting with the SiO$^-$ site. It implies that the hydrogen bonding of the H-down OH in SL at low pH is slightly weaker than that of the water OH interacting with the SiO$^-$ site. This negative OH band is attributable to the H-down water OH that accepts hydrogen bonding from the SiOH site and/or the OH of the SiOH site itself because these OHs highly likely exhibit a low-frequency negative band due to the strong hydrogen bonding. It is noted that Tuladhar et al. recently reported a DFT-based molecular dynamics simulation that suggested that the negative OH band observed at pH 2.0 are contributed 76% by water and 24% by silanol.[62] The Im$\chi^{(2)}_{SL,SpAcidic}$ spectrum also exhibits a minor positive OH band in the high-frequency region around 3650 cm^{-1}. This positive band is assignable to the OH groups that are weakly interacting with a surface site that can form weak hydrogen bonding only at low pH. This pH-dependent weak hydrogen-bonding site is considered to be the O atom of the pH-dependent SiOH site rather than the O atom of the pH-independent siloxane bridges (Si−O−Si).[63]

4. DISCUSSION

4.1. Structure of EDL at the Silica/Water Interface. Based on the results of the experiments and analyses described in Section 3, we first discuss the structure of EDL at the silica/water interface. The water spectrum of DL (Im$\chi^{(2)}_{DL}$) (black line in Figure 6A) shows a major OH band similar to the bulk water spectra and exhibits a doublet feature (peaked at ∼3200 and ∼3450 cm^{-1}). The spectral similarity to the bulk water indicates that the hydrogen-bonding structure of water in DL is not significantly changed by the electric field/Coulomb forces arising from the charge at the silica surface. This experimental observation is consistent with the prediction of theoretical studies.[41,42] Our previous HD-VSFG study revealed that the doublet feature of the band disappears with isotopic dilution.[39] Therefore, it arises from the vibrational coupling such as Fermi resonance but not from different water structures, although the two peaks were sometimes called "ice-like" and "liquid-like" bands in the literature.[20,37,64]

The water spectra of SL (Im$\chi^{(2)}_{SL}$) at different pH are independent from the NaCl concentration in the range from 0.01 to 2.0 M at each pH, and they can be decomposed into

https://doi.org/10.1021/jacs.2c11344
J. Am. Chem. Soc. 2023, 145, 8833−8846

three spectral components, that is, $\mathrm{Im}\chi^{(2)}_{\mathrm{SL,SpBasic}}$, $\mathrm{Im}\chi^{(2)}_{\mathrm{SL,SpAcidic}}$, and $\mathrm{Im}\chi^{(2)}_{\mathrm{SL,SpNeutral}}$ which are shown with red, blue, and green lines in Figure 6A, respectively. In some conventional VSFG studies, the bands peaked at 3200 and 3400 cm^{-1} were assigned to water in DL and SL, respectively,[24,27,48] but the present HD-VSFG study clearly shows both $\mathrm{Im}\chi^{(2)}_{\mathrm{DL}}$ and $\mathrm{Im}\chi^{(2)}_{\mathrm{SL}}$ have substantial amplitude around 3200 cm^{-1}. Furthermore, the SVD analysis of pH-dependent $\mathrm{Im}\chi^{(2)}_{\mathrm{SL}}$ indicates that there is contribution from $\mathrm{Im}\chi^{(2)}_{\mathrm{SL,SpNeutral}}$ at all pHs, although the amplitudes of $\mathrm{Im}\chi^{(2)}_{\mathrm{SL}}$ at ∼3400 cm^{-1} at high and low pH regions are small because of the cancellation of different spectral components.

The $\mathrm{Im}\chi^{(2)}_{\mathrm{SL}}$ spectra and their three spectral components are very different from the $\mathrm{Im}\chi^{(2)}_{\mathrm{DL}}$ spectrum (Figures 3 and 6). This demonstrates that the direct interaction between the silica surface and the water molecules in SL is much stronger than the effect of the electric field/Coulomb forces on the water in DL. Two strong interactions with the silica surface are possible for water in SL: hydrogen bonding (10−35 kJ/mol)[65,66] and charge−dipole interactions (3−18 kJ/mol).[67,68] In particular, under basic pH conditions where the silica surface is abundant with SiO^- sites, both interactions with negatively charged SiO^- sites can induce the orientation of one OH of the water molecule toward the silica surface in SL, giving rise to the $\mathrm{Im}\chi^{(2)}_{\mathrm{SL,SpBasic}}$ component in the $\mathrm{Im}\chi^{(2)}_{\mathrm{SL}}$ spectra. On the other hand, under acidic pH conditions, the silica surface is abundant with SiOH sites, and the neutral SiOH acts as the hydrogen-bond donor to induce the OH orientation of water molecules away from the silica surface in SL, as indicated by the $\mathrm{Im}\chi^{(2)}_{\mathrm{SL,SpAcidic}}$ component (Figure 6).

4.2. Surface Charge and pK_a of the Silica Surface. The analysis described in Section 3.2 shows that a significant increase in the surface charge density occurs only at around pH 5.0 (Figure 4E). In the past, several homodyne SHG studies reported multiple pK_a values for the protonation/deprotonation equilibrium at the silica surface based on the two- or three-step increases of the SHG intensity observed with varying pH.[9,25,28] In these SHG studies, the SHG intensity was directly related to the surface potential ϕ_0 under the assumption of the simple GC theory, without separating the contribution from SL and DL. This way of estimating the pK_a value seems unreliable because of the co-existence of the $\chi^{(2)}_{\mathrm{SL}}$ and $\chi^{(2)}_{\mathrm{DL}}$ contributions in total intensity. Indeed, the first (lower) pK_a indicated by the SHG studies is roughly consistent with the pK_a determined from the separated $\mathrm{Im}\chi^{(2)}_{\mathrm{DL}}$ contribution in the present study, whereas the apparent second (higher) pK_a suggested by the SHG data seems to correspond to the changes in the $\mathrm{Im}\chi^{(2)}_{\mathrm{SL}}$ contribution observed in our data. Because the relationship between the charge density σ_0 and $\mathrm{Im}\chi^{(2)}_{\mathrm{SL}}$ is not clear at the moment, it can be said that, only after separating the $\mathrm{Im}\chi^{(2)}_{\mathrm{SL}}$ contribution, we can safely evaluate the pH dependence of the charge density σ_0 and the pK_a value of the silica surface from the pH-dependent $\mathrm{Im}\chi^{(2)}_{\mathrm{DL}}$ signal.

We note that the pH dependences of the $\mathrm{Im}\chi^{(2)}_{\mathrm{DL}}$ amplitude of different substrates also show no noticeable increase in the high pH region, indicating a single pK_a value around pH 5.0 (Figure S9A), although the $\mathrm{Im}\chi^{(2)}_{\mathrm{DL}}$ amplitude itself exhibits some deviations. Similar behaviors of the zeta potential (ϕ_ζ), which increases significantly around pH 5.0 and saturates between pH 6.0 and pH 9.0, have been reported for silica particles.[69−73] The zeta potential ϕ_ζ is known as the potential at the shear plane of DL, which is proportional to the Stern potential ϕ_S ($\phi_\zeta \propto \phi_S$).[74−76] This similarity between pH dependences of ϕ_ζ and $\mathrm{Im}\chi^{(2)}_{\mathrm{DL}}$ also validates our analysis of the $\mathrm{Im}\chi^{(2)}_{\mathrm{DL}}$ spectra and the pK_a value obtained. Thus, we emphasize the importance of separately discussing the DL and SL spectra as well as their pH dependences to obtain a proper/accurate understanding.

The separate discussion of pH-dependent change of the $\mathrm{Im}\chi^{(2)}_{\mathrm{DL}}$ and $\mathrm{Im}\chi^{(2)}_{\mathrm{SL}}$ also helps us to think about the arguments made in other previous studies. As seen in Figure S11A in the Supporting Information, the integrated $|\chi^{(2)}|^2$ intensity exhibits a decrease-then-increase pH dependence with $C_0 \geq 0.1$ M. Such a dependence originates from the sign-flip of the $\mathrm{Im}\chi^{(2)}$ amplitude (Figure S11B). In previous conventional homodyne-detected VSFG studies, the sign-flip of the DL component was claimed to explain the decrease-then-increase pH dependence of the VSFG intensity ($I_{\mathrm{SFG}} \propto |\chi^{(2)}|^2$).[48,56] However, the silica surface is negatively charged from pH 2.0 to pH 12.0, as shown by the positive $\mathrm{Im}\chi^{(2)}_{\mathrm{DL}}$ amplitudes in the present study (Figures S6 and S11C) and the zeta potential reported.[69−73] Thus, it is clear that the sign-flip of $\mathrm{Im}\chi^{(2)}$ solely originates from the sign-flip of $\mathrm{Im}\chi^{(2)}_{\mathrm{SL}}$ (Figure S11D) rather than the charge reversal of the silica surface during the pH titration. The $\mathrm{Im}\chi^{(2)}_{\mathrm{DL}}$ always appears with a positive sign in the NaCl concentration range of 0.01−2.0 M at all pHs, revealing that no charge reversal occurs with the addition of NaCl. These results also clearly negate the charge reversal of the silica surface at different NaCl concentrations, which was proposed in a simulation study.[57]

The pH dependence of the $\mathrm{Im}\chi^{(2)}_{\mathrm{SL}}$ spectra described in Section 3.3 also brought new insights into the pH-dependent spectra of the water in the vicinity of the silica surface. As shown in Figure 5A, the $\mathrm{Im}\chi^{(2)}_{\mathrm{SL}}$ spectra show significant change only for the low-frequency OH bands (∼3200 cm^{-1}), which reflect strong hydrogen bonding with the silica surface. The sign inversion of the total $\mathrm{Im}\chi^{(2)}_{\mathrm{SL}}$ amplitude at around pH 5.0 (Figure S11D) is mainly caused by the sign flipping of this low-frequency OH band. This result strongly indicates that the sign of the $\mathrm{Im}\chi^{(2)}_{\mathrm{SL}}$ spectrum is not simply determined by the charge and potential at the silica surface. Therefore, it is safe to say that the sign inversion of the net $\mathrm{Im}\chi^{(2)}_{\mathrm{SL}}$ amplitude at around pH 5.0 occurs as the result of the balance between the hydrogen bonding and charge−dipole interactions in SL rather than the reversal of the charge or potential within the SL.

4.3. pH-Dependence of Water Structures in DL and SL. Finally, we discuss the pH-dependent water structure in DL and SL. The absolute amplitudes of $\mathrm{Im}\chi^{(2)}_{\mathrm{DL}}$ and the three spectral components of $\mathrm{Im}\chi^{(2)}_{\mathrm{SL}}$ ($\mathrm{Im}\chi^{(2)}_{\mathrm{SL,SpAcidic}}$, $\mathrm{Im}\chi^{(2)}_{\mathrm{SL,SpNeutral}}$, and $\mathrm{Im}\chi^{(2)}_{\mathrm{SL,SpBasic}}$) are plotted against pH in Figure 6B, which are obtained by integrating the absolute spectral amplitude in the frequency range of 2900−3800 cm^{-1} at each pH. This plot represents how the population of the corresponding water species changes in DL and SL, depending on pH.

The $\mathrm{Im}\chi^{(2)}$ spectrum of the silica/water interface at pH 2.0 is dominated by the contribution of $\mathrm{Im}\chi^{(2)}_{\mathrm{SL,SpAcidic}}$. As the pH increases from pH 2.0 to 6.0, the amplitude of the $\mathrm{Im}\chi^{(2)}_{\mathrm{SL,SpAcidic}}$ decreases, whereas the amplitude of $\mathrm{Im}\chi^{(2)}_{\mathrm{DL}}$ increases. The change of these amplitudes is both attributed to the deprotonation of the SiOH site: the decreases of the $\mathrm{Im}\chi^{(2)}_{\mathrm{SL,SpAcidic}}$ amplitude reflect the decrease of the surface SiOH density that causes the decrease of the water species that accepts hydrogen-bonding from the OH of SiOH, while the increases of the $\mathrm{Im}\chi^{(2)}_{\mathrm{DL}}$ amplitude arise from the increase of the surface SiO^- density due to the deprotonation of the SiOH,

https://doi.org/10.1021/jacs.2c11344
J. Am. Chem. Soc. 2023, 145, 8833−8846

which generates a stronger electric field and hence induces more oriented water in DL.

Interestingly, the amplitudes of $\mathrm{Im}\chi^{(2)}_{\mathrm{SL,SpAcidic}}$ and $\mathrm{Im}\chi^{(2)}_{\mathrm{SL,SpBasic}}$ are both practically zero, and the contribution of the small $\mathrm{Im}\chi^{(2)}_{\mathrm{SL,SpNeutral}}$ component dominates $\mathrm{Im}\chi^{(2)}_{\mathrm{DL}}$ in the neutral pH region (pH 6.0 to 7.5), although the pH-dependent amplitude of $\mathrm{Im}\chi^{(2)}_{\mathrm{DL}}$ indicates that the surface charge density is almost saturated at neutral pH. It means that the water in SL has the least net orientation at the neutral pH region, even though the silica surface is negatively charged. This surprising result indicates that the water structure in SL changes collectively rather than each water molecule separately interacting with the surface sites (SiO^- or SiOH), particularly in the neutral pH region.

As the pH increases from pH 7.5 to pH 12.0, the amplitude of $\mathrm{Im}\chi^{(2)}_{\mathrm{SL,SpBasic}}$ increases. The growth of the $\mathrm{Im}\chi^{(2)}_{\mathrm{SL,SpBasic}}$ amplitude indicates the orientational ordering of the SL water is enhanced in the basic pH region as pH becomes higher. This $\mathrm{Im}\chi^{(2)}_{\mathrm{SL,SpBasic}}$ spectrum corresponds to the water molecules forming strong hydrogen bonding under the high electric field at the charged surface.[13] It is intriguing that the water ordering in SL is greatly enhanced, although the DL water contribution ($\mathrm{Im}\chi^{(2)}_{\mathrm{DL}}$) shows a small decrease at pH 12.0. Such a small decrease in the $\mathrm{Im}\chi^{(2)}_{\mathrm{DL}}$ amplitude is also observed for other silica substrates (Figure S9A). The reason for this observation is not clear at the moment, but it seems that it arises from a phenomenon beyond the MGC theory, such as an increase in the number of Na^+ in SL and/or a change in the thickness of SL (Z_{SL}). Such changes would cause a decrease in the Stern potential ϕ_{S} and the $\mathrm{Im}\chi^{(2)}_{\mathrm{DL}}$ contribution at pH 12.0, leading to a noticeable decrease in the estimated σ_0 value at this pH (Figure 4E).

As mentioned earlier, the amplitude of $\mathrm{Im}\chi^{(2)}_{\mathrm{DL}}$ exhibits substantial substrate dependence (Figure S9A), whereas the amplitude of $\mathrm{Im}\chi^{(2)}_{\mathrm{SL}}$ shows almost no noticeable variation (Figure S9B). The Stern layer spectral components obtained from the SVD analysis of different silica substrates (Figure S10C) also show no noticeable variations. These observations support that the amplitude of $\mathrm{Im}\chi^{(2)}_{\mathrm{SL}}$ does not simply reflect the potential of the silica surface that is proportional to the $\mathrm{Im}\chi^{(2)}_{\mathrm{DL}}$ amplitude but is determined by the multiple properties and interactions appearing in SL.

The molecular picture of water structure in EDL and its pH-dependent changes obtained in this study are illustrated in Figure 6C.

While we were preparing the manuscript of this paper, a combined HD-SHG and conventional VSFG study on the silica/water interface was reported by the Gibbs group and the Geiger group.[77] In their paper, the $\mathrm{Im}\chi^{(2)}$ spectra at different pH were calculated from homodyne VSFG spectra using the MEM analysis, referring to the $\mathrm{Im}\chi^{(2)}$ spectra reported by our group[39] for a phase reference. Then, using the measured zeta potential ϕ_ζ and the $\mathrm{Im}\chi^{(2)}_{\mathrm{DL}}$ spectral shape reported in literature,[39] they estimated the $\mathrm{Im}\chi^{(2)}_{\mathrm{DL}}$ spectral contributions at different pH and calculated the $\mathrm{Im}\chi^{(2)}_{\mathrm{SL}}$ spectra by subtracting the estimated $\mathrm{Im}\chi^{(2)}_{\mathrm{DL}}$ at each pH. The pH dependences of the $\mathrm{Im}\chi^{(2)}_{\mathrm{DL}}$ and $\mathrm{Im}\chi^{(2)}_{\mathrm{SL}}$ spectra in their paper fairly accord with the pH dependences obtained in the present study, in particular at high pH and low pH. The basically consistent results obtained with very different approaches assure the validity of these two approaches and the obtained results. Yet, they did not decompose the SL water spectra into the spectra of each SL water species and did not quantitatively discuss the pH-dependent change of their populations. We emphasize that, in the present work, the $\mathrm{Im}\chi^{(2)}$ spectra were directly obtained from the HD-VSFG measurements, and the $\mathrm{Im}\chi^{(2)}_{\mathrm{DL}}$ and $\mathrm{Im}\chi^{(2)}_{\mathrm{SL}}$ spectra were obtained by the model-free separation using SVD analysis. Therefore, these spectra are free from any assumptions and theoretical models. We stress that this model-free approach allowed us to decompose the $\mathrm{Im}\chi^{(2)}_{\mathrm{SL}}$ spectra into three spectral components and provide detailed, solid information about EDL at the silica/water interface, highlighting the advantage of the direct HD-VSFG measurements.

5. SUMMARY

In this study, we measured the $\mathrm{Im}\chi^{(2)}$ spectra of the buried silica/water interface in a wide pH range (pH 2.0−pH 12.0) with changing the salt concentration (0.01−5.0 M). Taking full advantage of the $\mathrm{Im}\chi^{(2)}$ spectra, we analyzed the obtained spectra using SVD to elucidate the structure of EDL at the silica/water interface. It was found that the $\mathrm{Im}\chi^{(2)}$ spectra can be decomposed into the spectra of DL and SL ($\mathrm{Im}\chi^{(2)}_{\mathrm{DL}}$ and $\mathrm{Im}\chi^{(2)}_{\mathrm{SL}}$), demonstrating that the EDL is well described by the Stern model. Furthermore, this spectral decomposition enabled us to quantitatively analyze the water in different parts of the EDL. The positive $\mathrm{Im}\chi^{(2)}_{\mathrm{DL}}$ spectra at all pHs ranging from pH 2.0 to 12.0 indicate that the silica/water interface is negatively charged in the entire pH range investigated. Quantitative analysis of the pH- and salt-dependences of the amplitude of $\mathrm{Im}\chi^{(2)}_{\mathrm{DL}}$ provides only one single pK_a value of $pK_a = 4.8 \pm 0.2$ with the use of the MGC theory. It was also found that the SL is fully formed at a low salt concentration (0.01 M), and the SL is unchanged up to the salt concentration as high as 2.0 M at all pH examined. The pH-dependent change of $\mathrm{Im}\chi^{(2)}_{\mathrm{SL}}$ is quantitatively explained with the pH-dependent change of the amplitude of the three spectral components ($\mathrm{Im}\chi^{(2)}_{\mathrm{SL,SpAcidic}}$, $\mathrm{Im}\chi^{(2)}_{\mathrm{SL,SpBasic}}$, and $\mathrm{Im}\chi^{(2)}_{\mathrm{SL,SpNeutral}}$) that represent three different types of water species in SL adjacent to the silica surface. The three water species show distinctive OH orientations and pH-dependent populations, originating from the competition/balance between hydrogen bonding and charge−dipole interaction. These clear molecular pictures of the EDL at the silica/water interface were obtainable only with $\mathrm{Im}\chi^{(2)}$ spectra that are linear to the second-order nonlinear molecular response, which affords the additivity of multiple spectral components and allows us to rigorously use SVD analysis. The present study not only provides a clear molecular picture of EDL at the silica/water interface but also demonstrates the importance and strength of HD-VSFG in investigating various interfaces, including buried interfaces.

■ ASSOCIATED CONTENT

Supporting Information

The Supporting Information is available free of charge at https://pubs.acs.org/doi/10.1021/jacs.2c11344.

Optical configuration of the HD-VSFG setup, correction of the $\chi^{(2)}$ spectra for the Fresnel factor and reflectivity, singular value decomposition (SVD) analysis, salt-concentration dependence of the bulk water spectra and the SVD analysis, modified Gouy−Chapman (MGC) theory, substrate dependence of the DL and SL spectra, normalized difference SL spectra at high pH and low pH, and pH dependence of the integrated $|\chi^{(2)}|^2$ intensity and integrated $\mathrm{Im}\chi^{(2)}$ amplitude (PDF)

https://doi.org/10.1021/jacs.2c11344
J. Am. Chem. Soc. 2023, 145, 8833−8846

AUTHOR INFORMATION

Corresponding Author

Tahei Tahara − *Molecular Spectroscopy Laboratory, RIKEN, Wako, Saitama 351-0198, Japan; Ultrafast Spectroscopy Research Team, RIKEN Center for Advanced Photonics (RAP), Wako, Saitama 351-0198, Japan;* orcid.org/0000-0002-6340-8535; Email: tahei@riken.jp

Authors

Feng Wei − *Molecular Spectroscopy Laboratory, RIKEN, Wako, Saitama 351-0198, Japan;* Present Address: Institute of Interdisciplinary Research & School of Optoelectronic Materials and Technology, Jianghan University, Wuhan 430056, China; orcid.org/0000-0002-3218-5754

Shu-hei Urashima − *Molecular Spectroscopy Laboratory, RIKEN, Wako, Saitama 351-0198, Japan;* Present Address: Tokyo University of Science, Kagurazaka, Shinjuku, Tokyo, 162-8601, Japan.; orcid.org/0000-0001-8772-4287

Satoshi Nihonyanagi − *Molecular Spectroscopy Laboratory, RIKEN, Wako, Saitama 351-0198, Japan; Ultrafast Spectroscopy Research Team, RIKEN Center for Advanced Photonics (RAP), Wako, Saitama 351-0198, Japan;* orcid.org/0000-0003-0014-7427

Complete contact information is available at: https://pubs.acs.org/10.1021/jacs.2c11344

Author Contributions

The manuscript was written through the contributions of all authors. All authors have approved the final version of the manuscript.

Notes

The authors declare no competing financial interest.

ACKNOWLEDGMENTS

This work was supported by the JSPS KAKENHI grant number 18H05265.

REFERENCES

(1) Tang, M.; Cziczo, D. J.; Grassian, V. H. Interactions of Water with Mineral Dust Aerosol: Water Adsorption, Hygroscopicity, Cloud Condensation, and Ice Nucleation. *Chem. Rev.* **2016**, *116*, 4205−4259.

(2) Minakata, S.; Komatsu, M. Organic Reactions on Silica in Water. *Chem. Rev.* **2008**, *109*, 711−724.

(3) Lorenz, C. D.; Crozier, P. S.; Anderson, J. A.; Travesset, A. Molecular Dynamics of Ionic Transport and Electrokinetic Effects in Realistic Silica Channels. *J. Phys. Chem. C* **2008**, *112*, 10222−10232.

(4) Jafari, S.; Derakhshankhah, H.; Alaei, L.; Fattahi, A.; Varnamkhasti, B. S.; Saboury, A. A. Mesoporous silica nanoparticles for therapeutic/diagnostic applications. *Biomed. Pharmacother.* **2019**, *109*, 1100−1111.

(5) Walcarius, A. Silica-based electrochemical sensors and biosensors: Recent trends. *Curr. Opin. Electrochem.* **2018**, *10*, 88−97.

(6) Iler, R. K. *The Chemistry of Silica. Solubility, Polymerization, Colloid and Surface Properties, and Biochemistry*; John Wiley & Sons Inc., 1979; p 896.

(7) Barisik, M.; Atalay, S.; Beskok, A.; Qian, S. Size Dependent Surface Charge Properties of Silica Nanoparticles. *J. Phys. Chem. C* **2014**, *118*, 1836−1842.

(8) Aveyard, R.; Haydon, D. A. *An Introduction to the Principles of Surface Chemistry*; Cambridge University Press, 1973; p 248.

(9) Ong, S.; Zhao, X.; Eisenthal, K. B. Polarization of water molecules at a charged interface: second harmonic studies of the silica/water interface. *Chem. Phys. Lett.* **1992**, *191*, 327−335.

(10) Kilic, M. S.; Bazant, M. Z.; Ajdari, A. Steric effects in the dynamics of electrolytes at large applied voltages. I. Double-layer charging. *Phys. Rev. E* **2007**, *75*, 021502.

(11) Borukhov, I.; Andelman, D.; Orland, H. Steric Effects in Electrolytes: A Modified Poisson-Boltzmann Equation. *Phys. Rev. Lett.* **1997**, *79*, 435−438.

(12) Alfarano, S. R.; Pezzotti, S.; Stein, C. J.; Lin, Z.; Sebastiani, F.; Funke, S.; Hoberg, C.; Kolling, I.; Ma, C. Y.; Mauelshagen, K.; Ockelmann, T.; Schwaab, G.; Fu, L.; Brubach, J.-B.; Roy, P.; Head-Gordon, M.; Tschulik, K.; Gaigeot, M.-P.; Havenith, M. Stripping away ion hydration shells in electrical double-layer formation: Water networks matter. *Proc. Natl. Acad. Sci. U.S.A.* **2021**, *118*, No. e2115539118.

(13) Grahame, D. C. The Electrical Double Layer and the Theory of Electrocapillarity. *Chem. Rev.* **2002**, *41*, 441−501.

(14) Velasco-Velez, J.-J.; Wu, C. H.; Pascal, T. A.; Wan, L. F.; Guo, J.; Prendergast, D.; Salmeron, M. The structure of interfacial water on gold electrodes studied by x-ray absorption spectroscopy. *Science* **2014**, *346*, 831−834.

(15) Favaro, M.; Jeong, B.; Ross, P. N.; Yano, J.; Hussain, Z.; Liu, Z.; Crumlin, E. J. Unravelling the electrochemical double layer by direct probing of the solid/liquid interface. *Nat. Commun.* **2016**, *7*, 12695.

(16) Richmond, G. L.; Rojhantalab, H. M.; Robinson, J. M.; Shannon, V. L. Experiments on optical second-harmonic generation as a surface probe of electrodes. *J. Opt. Soc. Am. B* **1987**, *4*, 228−236.

(17) Chen, C. K.; Heinz, T. F.; Ricard, D.; Shen, Y. R. Detection of Molecular Monolayers by Optical Second-Harmonic Generation. *Phys. Rev. Lett.* **1981**, *46*, 1010−1012.

(18) Ma, E.; Geiger, F. M. Divalent Ion Specific Outcomes on Stern Layer Structure and Total Surface Potential at the Silica: Water Interface. *J. Phys. Chem. A* **2021**, *125*, 10079−10088.

(19) Du, Q.; Freysz, E.; Shen, Y. R. Vibrational spectra of water molecules at quartz/water interfaces. *Phys. Rev. Lett.* **1994**, *72*, 238−241.

(20) Ostroverkhov, V.; Waychunas, G. A.; Shen, Y. R. Vibrational spectra of water at water/α-quartz (0001) interface. *Chem. Phys. Lett.* **2004**, *386*, 144−148.

(21) Ohno, P. E.; Wang, H.-f.; Geiger, F. M. Second-order spectral lineshapes from charged interfaces. *Nat. Commun.* **2017**, *8*, 1032.

(22) Rey, N. G.; Dlott, D. D. Studies of electrochemical interfaces by broadband sum frequency generation. *J. Electroanal. Chem.* **2017**, *800*, 114−125.

(23) Wen, Y.-C.; Zha, S.; Liu, X.; Yang, S.; Guo, P.; Shi, G.; Fang, H.; Shen, Y. R.; Tian, C. Unveiling Microscopic Structures of Charged Water Interfaces by Surface-Specific Vibrational Spectroscopy. *Phys. Rev. Lett.* **2016**, *116*, 016101.

(24) Jena, K. C.; Covert, P. A.; Hore, D. K. The Effect of Salt on the Water Structure at a Charged Solid Surface: Differentiating Second- and Third-order Nonlinear Contributions. *J. Phys. Chem. Lett.* **2011**, *2*, 1056−1061.

(25) Azam, M. S.; Weeraman, C. N.; Gibbs-Davis, J. M. Specific Cation Effects on the Bimodal Acid−Base Behavior of the Silica/Water Interface. *J. Phys. Chem. Lett.* **2012**, *3*, 1269−1274.

(26) Azam, M. S.; Weeraman, C. N.; Gibbs-Davis, J. M. Halide-Induced Cooperative Acid−Base Behavior at a Negatively Charged Interface. *J. Phys. Chem. C* **2013**, *117*, 8840−8850.

(27) Covert, P. A.; Jena, K. C.; Hore, D. K. Throwing Salt into the Mix: Altering Interfacial Water Structure by Electrolyte Addition. *J. Phys. Chem. Lett.* **2014**, *5*, 143−148.

(28) Darlington, A. M.; Gibbs-Davis, J. M. Bimodal or Trimodal? The Influence of Starting pH on Site Identity and Distribution at the Low Salt Aqueous/Silica Interface. *J. Phys. Chem. C* **2015**, *119*, 16560−16567.

(29) Backus, E. H. G.; Schaefer, J.; Bonn, M. Probing the Mineral−Water Interface with Nonlinear Optical Spectroscopy. *Angew. Chem., Int. Ed.* **2020**, *60*, 10482−10501.

(30) Borukhov, I.; Andelman, D.; Orland, H. Adsorption of large ions from an electrolyte solution: a modified Poisson−Boltzmann equation. *Electrochim. Acta* **2000**, *46*, 221−229.
(31) Gongadze, E.; Rienen, U.; Iglič, A. Generalized stern models of the electric double layer considering the spatial variation of permittvity and finite size of ions in saturation regime. *Cell. Mol. Biol. Lett.* **2011**, *16*, 576−594.
(32) Sulpizi, M.; Gaigeot, M. P.; Sprik, M. The Silica-Water Interface: How the Silanols Determine the Surface Acidity and Modulate the Water Properties. *J. Chem. Theory Comput.* **2012**, *8*, 1037−1047.
(33) Eftekhari-Bafrooei, A.; Borguet, E. Effect of Electric Fields on the Ultrafast Vibrational Relaxation of Water at a Charged Solid−Liquid Interface as Probed by Vibrational Sum Frequency Generation. *J. Phys. Chem. Lett.* **2011**, *2*, 1353−1358.
(34) Lovering, K. A.; Bertram, A. K.; Chou, K. C. New Information on the Ion-Identity-Dependent Structure of Stern Layer Revealed by Sum Frequency Generation Vibrational Spectroscopy. *J. Phys. Chem. C* **2016**, *120*, 18099−18104.
(35) Nihonyanagi, S.; Mondal, J. A.; Yamaguchi, S.; Tahara, T. Structure and Dynamics of Interfacial Water Studied by Heterodyne-Detected Vibrational Sum-Frequency Generation. *Annu. Rev. Phys. Chem.* **2013**, *64*, 579−603.
(36) Shen, Y. R. Phase-Sensitive Sum-Frequency Spectroscopy. *Annu. Rev. Phys. Chem.* **2013**, *64*, 129−150.
(37) Ostroverkhov, V.; Waychunas, G. A.; Shen, Y. R. New information on water interfacial structure revealed by phase-sensitive surface spectroscopy. *Phys. Rev. Lett.* **2005**, *94*, 046102.
(38) Nihonyanagi, S.; Yamaguchi, S.; Tahara, T. Direct evidence for orientational flip-flop of water molecules at charged interfaces: a heterodyne-detected vibrational sum frequency generation study. *J. Chem. Phys.* **2009**, *130*, 204704.
(39) Myalitsin, A.; Urashima, S.; Nihonyanagi, S.; Yamaguchi, S.; Tahara, T. Water Structure at the Buried Silica/Aqueous Interface Studied by Heterodyne-Detected Vibrational Sum-Frequency Generation. *J. Phys. Chem. C* **2016**, *120*, 9357−9363.
(40) Urashima, S.; Myalitsin, A.; Nihonyanagi, S.; Tahara, T. The Topmost Water Structure at a Charged Silica/Aqueous Interface Revealed by Heterodyne-Detected Vibrational Sum Frequency Generation Spectroscopy. *J. Phys. Chem. Lett.* **2018**, *9*, 4109−4114.
(41) Joutsuka, T.; Hirano, T.; Sprik, M.; Morita, A. Effects of third-order susceptibility in sum frequency generation spectra: a molecular dynamics study in liquid water. *Phys. Chem. Chem. Phys.* **2018**, *20*, 3040−3053.
(42) Pezzotti, S.; Galimberti, D. R.; Gaigeot, M.-P. Deconvolution of BIL-SFG and DL-SFG spectroscopic signals reveals order/disorder of water at the elusive aqueous silica interface. *Phys. Chem. Chem. Phys.* **2019**, *21*, 22188−22202.
(43) Rehl, B.; Gibbs, J. M. Role of Ions on the Surface-Bound Water Structure at the Silica/Water Interface: Identifying the Spectral Signature of Stability. *J. Phys. Chem. Lett.* **2021**, *12*, 2854−2864.
(44) Ahmed, M.; Nihonyanagi, S.; Tahara, T. Ultrafast vibrational dynamics of the free OD at the air/water interface: Negligible isotopic dilution effect but large isotope substitution effect. *J. Chem. Phys.* **2022**, *156*, 224701.
(45) Kumar, P.; Fron, E.; Hosoi, H.; Kuramochi, H.; Takeuchi, S.; Mizuno, H.; Tahara, T. Excited-State Proton Transfer Dynamics in LSSmOrange Studied by Time-Resolved Impulsive Stimulated Raman Spectroscopy. *J. Phys. Chem. Lett.* **2021**, *12*, 7466−7473.
(46) Fujisawa, T.; Masuda, S.; Takeuchi, S.; Tahara, T. Femtosecond Time-Resolved Absorption Study of Signaling State of a BLUF Protein PixD from the Cyanobacterium Synechocystis: Hydrogen-Bond Rearrangement Completes during Forward Proton-Coupled Electron Transfer. *J. Phys. Chem. B* **2021**, *125*, 12154−12165.
(47) Yang, Z.; Li, Q.; Chou, K. C. Structures of Water Molecules at the Interfaces of Aqueous Salt Solutions and Silica: Cation Effects. *J. Phys. Chem. C* **2009**, *113*, 8201−8205.
(48) Darlington, A. M.; Jarisz, T. A.; DeWalt-Kerian, E. L.; Roy, S.; Kim, S.; Azam, M. S.; Hore, D. K.; Gibbs, J. M. Separating the pH-Dependent Behavior of Water in the Stern and Diffuse Layers with Varying Salt Concentration. *J. Phys. Chem. C* **2017**, *121*, 20229−20241.
(49) Pezzotti, S.; Galimberti, D. R.; Shen, Y. R.; Gaigeot, M.-P. Structural definition of the BIL and DL: a new universal methodology to rationalize non-linear $\chi(2)(\omega)$ SFG signals at charged interfaces, including $\chi(3)(\omega)$ contributions. *Phys. Chem. Chem. Phys.* **2018**, *20*, 5190−5199.
(50) Ma, E.; Ohno, P. E.; Kim, J.; Liu, Y.; Lozier, E. H.; Miller, T. F.; Wang, H.-F.; Geiger, F. M. A New Imaginary Term in the Second-Order Nonlinear Susceptibility from Charged Interfaces. *J. Phys. Chem. Lett.* **2021**, *12*, 5649−5659.
(51) Antonio Alves Júnior, J.; Baptista Baldo, J. The Behavior of Zeta Potential of Silica Suspensions. *New J. Glass Ceram.* **2014**, *04*, 29−37.
(52) Schaefer, J.; Gonella, G.; Bonn, M.; Backus, E. H. G. Surface-specific vibrational spectroscopy of the water/silica interface: screening and interference. *Phys. Chem. Chem. Phys.* **2017**, *19*, 16875−16880.
(53) Ohno, P. E.; Saslow, S. A.; Wang, H. F.; Geiger, F. M.; Eisenthal, K. B. Phase-referenced nonlinear spectroscopy of the alpha-quartz/water interface. *Nat. Commun.* **2016**, *7*, 13587.
(54) Gonella, G.; Lütgebaucks, C.; de Beer, A. G. F.; Roke, S. Second Harmonic and Sum-Frequency Generation from Aqueous Interfaces Is Modulated by Interference. *J. Phys. Chem. C* **2016**, *120*, 9165−9173.
(55) Wang, H.-F. Sum frequency generation vibrational spectroscopy (SFG-VS) for complex molecular surfaces and interfaces: Spectral lineshape measurement and analysis plus some controversial issues. *Prog. Surf. Sci.* **2016**, *91*, 155−182.
(56) DeWalt-Kerian, E. L.; Kim, S.; Azam, M. S.; Zeng, H.; Liu, Q.; Gibbs, J. M. pH-Dependent Inversion of Hofmeister Trends in the Water Structure of the Electrical Double Layer. *J. Phys. Chem. Lett.* **2017**, *8*, 2855−2861.
(57) Chen, S.-H.; Singer, S. J. Molecular Dynamics Study of the Electric Double Layer and Nonlinear Spectroscopy at the Amorphous Silica−Water Interface. *J. Phys. Chem. B* **2019**, *123*, 6364−6384.
(58) Zhang, T.; Brantley, S. L.; Verreault, D.; Dhankani, R.; Corcelli, S. A.; Allen, H. C. Effect of pH and Salt on Surface pKa of Phosphatidic Acid Monolayers. *Langmuir* **2018**, *34*, 530−539.
(59) Dijkstra, T. W.; Duchateau, R.; van Santen, R. A.; Meetsma, A.; Yap, G. P. A. Silsesquioxane Models for Geminal Silica Surface Silanol Sites. A Spectroscopic Investigation of Different Types of Silanols. *J. Am. Chem. Soc.* **2002**, *124*, 9856−9864.
(60) Bistafa, C.; Surblys, D.; Kusudo, H.; Yamaguchi, Y. Water on hydroxylated silica surfaces: Work of adhesion, interfacial entropy, and droplet wetting. *J. Chem. Phys.* **2021**, *155*, 064703.
(61) Sauer, J.; Ugliengo, P.; Garrone, E.; Saunders, V. R. Theoretical Study of van der Waals Complexes at Surface Sites in Comparison with the Experiment. *Chem. Rev.* **1994**, *94*, 2095−2160.
(62) Tuladhar, A.; Dewan, S.; Pezzotti, S.; Brigiano, F. S.; Creazzo, F.; Gaigeot, M. P.; Borguet, E. Ions Tune Interfacial Water Structure and Modulate Hydrophobic Interactions at Silica Surfaces. *J. Am. Chem. Soc.* **2020**, *142*, 6991−7000.
(63) Cyran, J. D.; Donovan, M. A.; Vollmer, D.; Siro Brigiano, F.; Pezzotti, S.; Galimberti, D. R.; Gaigeot, M.-P.; Bonn, M.; Backus, E. H. G. Molecular hydrophobicity at a macroscopically hydrophilic surface. *Proc. Natl. Acad. Sci. U.S.A.* **2019**, *116*, 1520−1525.
(64) Shen, Y. R.; Ostroverkhov, V. Sum-frequency vibrational spectroscopy on water interfaces: Polar orientation of water molecules at interfaces. *Chem. Rev.* **2006**, *37*, 1140−1154.
(65) Saengsawang, O.; Remsungnen, T.; Fritzsche, S.; Haberlandt, R.; Hannongbua, S. Structure and Energetics of Water−Silanol Binding on the Surface of Silicalite-1: Quantum Chemical Calculations. *J. Phys. Chem. B* **2005**, *109*, 5684−5690.
(66) Smirnov, K. S. Structure and sum-frequency generation spectra of water on uncharged Q4 silica surfaces: a molecular dynamics study. *Phys. Chem. Chem. Phys.* **2020**, *22*, 2033−2045.

https://doi.org/10.1021/jacs.2c11344
J. Am. Chem. Soc. 2023, 145, 8833−8846

(67) Oh, M. I.; Gupta, M.; Weaver, D. F. Understanding Water Structure in an Ion-Pair Solvation Shell in the Vicinity of a Water/Membrane Interface. *J. Phys. Chem. B* **2019**, *123*, 3945−3954.
(68) Zhang, C.; Giberti, F.; Sevgen, E.; de Pablo, J. J.; Gygi, F.; Galli, G. Dissociation of salts in water under pressure. *Nat. Commun.* **2020**, *11*, 3037.
(69) Wang, X.; Alvarado, V. Kaolinite and Silica Dispersions in Low-Salinity Environments: Impact on a Water-in-Crude Oil Emulsion Stability. *Energies* **2011**, *4*, 1763−1778.
(70) Gun'ko, V.; Andriyko, L.; Zarko, V.; Marynin, A.; Olishevskyi, V.; Janusz, W. Effects of dissolved metal chlorides on the behavior of silica nanoparticles in aqueous media. *Open Chem.* **2014**, *12*, 480−491.
(71) Alkhammash, H. I.; Li, N.; Berthier, R.; de Planque, M. R. R. Native silica nanoparticles are powerful membrane disruptors. *Phys. Chem. Chem. Phys.* **2015**, *17*, 15547−15560.
(72) Chen, G.; Ni, Z.; Bai, Y.; Li, Q.; Zhao, Y. The role of interactions between abrasive particles and the substrate surface in chemical-mechanical planarization of Si-face 6H-SiC. *RSC Adv.* **2017**, *7*, 16938−16952.
(73) Jalil, A. H.; Pyell, U. Quantification of Zeta-Potential and Electrokinetic Surface Charge Density for Colloidal Silica Nanoparticles Dependent on Type and Concentration of the Counterion: Probing the Outer Helmholtz Plane. *J. Phys. Chem. C* **2018**, *122*, 4437−4453.
(74) Bhattacharjee, S. DLS and zeta potential − What they are and what they are not? *J. Controlled Release* **2016**, *235*, 337−351.
(75) Lowry, G. V.; Hill, R. J.; Harper, S.; Rawle, A. F.; Hendren, C. O.; Klaessig, F.; Nobbmann, U.; Sayre, P.; Rumble, J. Guidance to improve the scientific value of zeta-potential measurements in nanoEHS. *Environ. Sci.: Nano* **2016**, *3*, 953−965.
(76) Carrique, F.; Arroyo, F. J.; Delgado, A. V. Electrokinetics of Concentrated Suspensions of Spherical Colloidal Particles with Surface Conductance, Arbitrary Zeta Potential, and Double-Layer Thickness in Static Electric Fields. *J. Colloid Interface Sci.* **2002**, *252*, 126−137.
(77) Rehl, B.; Ma, E.; Parshotam, S.; DeWalt-Kerian, E. L.; Liu, T.; Geiger, F. M.; Gibbs, J. M. Water Structure in the Electrical Double Layer and the Contributions to the Total Interfacial Potential at Different Surface Charge Densities. *J. Am. Chem. Soc.* **2022**, *144*, 16338−16349.

https://doi.org/10.1021/jacs.2c11344
J. Am. Chem. Soc. 2023, 145, 8833−8846